INDIAN INSTITUTE OF TECHNOLOGY (BANARAS HINDU UNIVERSITY), VARANASI
भारतीय प्रौद्योगिकी संस्थान (काशी हिन्दू विश्वविद्यालय), वाराणसी
Serving the Nation Since 1919

Study of dynamic events on Solar Photosphere

A dissertation submitted to the Indian Institute of Technology (BHU) in partial fulfillment of the requirements for the Degree of

MASTERS OF TECHNOLOGY (INTEGRATED)
In
ENGINEERING PHYSICS

By
Sambit Kumar Giri
10410EN005
Department of Physics
Indian Institute of Technology (BHU) Varanasi

Supervised by
Dr.(Mrs.) Anita Mohan
Assistant Professor
Department of Physics
Indian Institute of Technology (BHU) Varanasi

Department of Physics
Indian Institute of Technology (BHU) Varanasi

Certificate

*This is to certify that the dissertation entitled **"Study of dynamic events on solar photosphere"** submitted in partial fulfillment of the requirements for the Degree of Masters of Technology (Integrated) in Engineering Physics, by **Sambit Kumar Giri** (Roll no. 10410EN005), is a bona-fide record of work carried by him under my supervision and guidance at the Department of Physics, Indian Institute of Technology (Banaras Hindu University) Varanasi.*

This is further certified that this work has not been submitted elsewhere for any degree or diploma.

Supervisor

[Dr.(Mrs.) Anita Mohan]
Asst. Professor
Department of Physics
Indian Institute of Technology (BHU)
Place: Date:

Approved for submission

[Dr. Debaprasad Giri]
Head of the Department
Department of Physics
Indian Institute of Technology (BHU)
Place: Date:

Undertaking

I, **Sambit Kumar Giri**, certify that the work embodied in this M.tech Dissertation is my own work carried under the supervision of **Dr.(Mrs.) Anita Mohan** for a period of 3 semesters from January 2014 to May 2015 at the Indian Institute of Technology (Banaras Hindu University) Varanasi and the matter embodied in this dissertation has not been submitted for the award of any other degree/diploma.
A part of this work was carried out at the Max Planck Institute for Solar System Research. The observations used in the work were recorded at Swedish 1-m Solar Telescope, located at La Palma, Spain.

I declare that I have faithfully acknowledged, given credit to and referred to the research workers wherever their works have been cited in the text and the body of the dissertation. I further certify that I have not willfully lifted any work, paragraphs, text, data, results etc. reported in the journals, books, magazines and reports available on websites and included them in the dissertation and cited as my own work.

Sambit Kumar Giri
10410EN005
IMD Part V, Engineering Physics
Department of Physics
IIT(BHU) Varanasi.

To my loving parents …

Acknowledgements

I would like to express my sincere gratitude to Dr.(Mrs.) Anita Mohan, Assistant Professor at Indian Institute of technology, Banaras Hindu University, Varanasi for giving me an opportunity to pursue this project under her expert guidance, active supervision and constant encouragement without which it would not have been possible to complete this project.

I would also like to express my deep gratitude to Prof. B. N. Dwivedi, Professor at Indian Institute of Technology, Banaras Hindu University, Varanasi for his valuable advice and resourceful guidance.

A part of the project was done in Max Planck Institute for Solar System Research. I am grateful to Prof. Sami Solanki and Dr. Michiel van Noort for providing me all the necessary facilities for the research and their expert advice on this project. The observations were made at the Swedish 1-m Solar Telescope, located at La Palma, Spain. I would like to thank Dr. Jayant Joshi and Dr. Gautam Narayan for the observations.

I sincerely thank the Head of Department, Dr. Debaprasad Giri, Assoc. Prof. Sandip Chatterji and all other faculty members and staff for helping me with this work and providing me assistance.

I also thank my family and all my friends for their constant support and helping me in believing in my abilities and capabilities.

Abstract

The sun is a very dynamic heavenly body. The magnetic field drives many small scale and large scale events. With the advent of better technology, we are able to observe the small-scale events occurring on the solar atmosphere. We have investigated the temporal evolution of a magnetohydrodynamic (MHD) surface waves propagating along the interface of bright point (BP) regions. This has been observed in the Active Region (AR) NOAA 11768 by inverting the spectropolarimetric data of photospheric Fe I (5250 Å) and C I (5380 Å), recorded by CRISP (CRisp Imaging SpectroPolarimeter) instrument at the Swedish 1-m Solar Telescope (SST). We make a horizontal velocity map of the region where the waves have been observed, which show a velocity discontinuity at the interface of BPs. The event is proposed to be caused due to the Kelvin-Helmholtz (KH) instability. A linear wave analysis of the magnetohydrodynamic (MHD) equations has been carried out taking account of KH instability to derive the dispersion relation. The results from the model have been compared with the observation. The phase velocity and the growth rate of the observed wave like pattern match with the values predicted by the model.

Table of contents

List of figures **xiii**

List of tables **xv**

1 Introduction **1**

- 1.1 Solar magnetic field 1
  - 1.1.1 Solar cycle 2
  - 1.1.2 Solar dynamo 4
  - 1.1.3 Magnetic field in convection zone 6
- 1.2 Lower Atmosphere 7
  - 1.2.1 Small-scale magnetic features 8
- 1.3 Spectropolarimetry 10

2 Instrumentation and Observation **15**

- 2.1 Swedish Solar Telescope 15
- 2.2 CRISP 17
- 2.3 Observations 17

3 Data Analysis **21**

- 3.1 Image restoration 21
  - 3.1.1 Seeing Error 21
  - 3.1.2 MOMFBD code 23
- 3.2 Event 23
- 3.3 Inversion Code 25
- 3.4 Destretching 25
- 3.5 Horizontal velocity field 26
  - 3.5.1 Shear velocity 27
  - 3.5.2 Phase speed 28
- 3.6 Amplitude growth 29

4 Theoretical model **33**
4.1 Magnetohydrodynamic Theory 33
4.2 Plasma Instability 36
  4.2.1 MHD instability 37
  4.2.2 Kelvin-Helmholtz instability 38
4.3 Proposed model 39

5 Discussion **43**
5.1 Numerical calculation 43
5.2 Observation and model 43
5.3 Further Implications 44

References **45**

List of figures

1.1 Sunspot Number 2
1.2 Butterfly Diagram 3
1.3 Solar Dynamo 6
1.4 Zeeman Splitting 12

2.1 Swedish Solar Telescope 16
2.2 CRISP 17
2.3 Wide-band Image 18

3.1 Wavefront Distortion 22
3.2 V/I 24
3.3 Patch containing the event 26
3.4 Horizontal Velocity 27
3.5 Shear Velocity 28
3.6 Tracking for Propagation Speed 29
3.7 Phase Velocity 30
3.8 Amplitude Growth 31

4.1 Coordinate System 40

List of tables

2.1 Observational parameters 18

Chapter 1

Introduction

Sun is a very mysterious star. Even though it is the closest of them all, it poses more questions than answers to the mechanism going on in an astronomical object. It is the primary source of energy on earth. Without sun, life cannot sustain on this planet. Even many molecules present in our body have been produced in the sun. From the age when the heliocentric model of Copernicus displaced the geocentric model to the standard solar model, our knowledge about the sun is increasing and improving.

In the ancient times, sun worship was very widespread. Among the Hindus, the sun god was one of the principal triad of deities, called *Surya* in Vedas. The sun for ancient Egyptian was God *Re*, a fiery disc in a boat across the sky. For Babylonians, the sun was a living being which moved against the solid vault of sky. With the appearance of reasonable deduction and cosmic perceptions, the sun was found to be one of a huge number of stars in the universe. The first noble gas of the periodic table, Helium, was found in sun before being found on earth. Individuals began concentrating on sun based occasions like solar eclipse, sunspot cycle, global oscillations of sun and so forth to build up a theoretical model of the sun.

In this chapter, the basic characteristics of the solar atmosphere has been outlined. The lower atmosphere has been discussed in more detail. Finally, the basic concepts of spectropolarimetry has been introduced.

1.1 Solar magnetic field

The solar magnetic field controls all the dynamics that happens in the Sun. Because of this control, the solar magnetic field influences atmosphere and climate of the earth. The sun oriented EUV radiation shifts in parallel with sunlight based movement cycle, being higher during maximum activity. The imperative features that can influence the sun oriented EUV radiation are faculae, pores, network and sunspots. The magnetic polarity of the global magnetic field switches at regular intervals. This gives a periodicity of 22-years, which is known as the solar cycle. The aggregate radiation likewise varies with the solar cycle.

The origin of the magnetic field in the solar atmosphere is still not known. Many theoretical models have been given to explain it, like, solar dynamo model. In this section, the magnetic field and it's effect has been discussed in more detail.

1.1.1 Solar cycle

The magnetic activity of the Sun, as most clear by the coming and fading of dark sunspots and the eruptive phenomena in the upper atmosphere and corona of the Sun, demonstrates a cyclic (however, not strictly periodic) variation with a mean time period of around 11 yr. There is a striking level of normality in the large-scale properties of this solar cycle, which underlies the apparently arbitrary appearance and evolution of the magnetic features in the turbulent surface layers of the Sun. The orderly inversions of the polar magnetic fields and the polarity orientation of sunspot group demonstrate that a complete magnetic cycle covers two 11-year action cycles.

Sunspot numbers

The longest precise direct record of solar activity is the series of sunspot numbers, which began not long after the creation of the telescope in the early 17th century. By compiling the records of numerous observers, it was conceivable to determine a series of sunspot numbers which reaches back to 1611 [1].

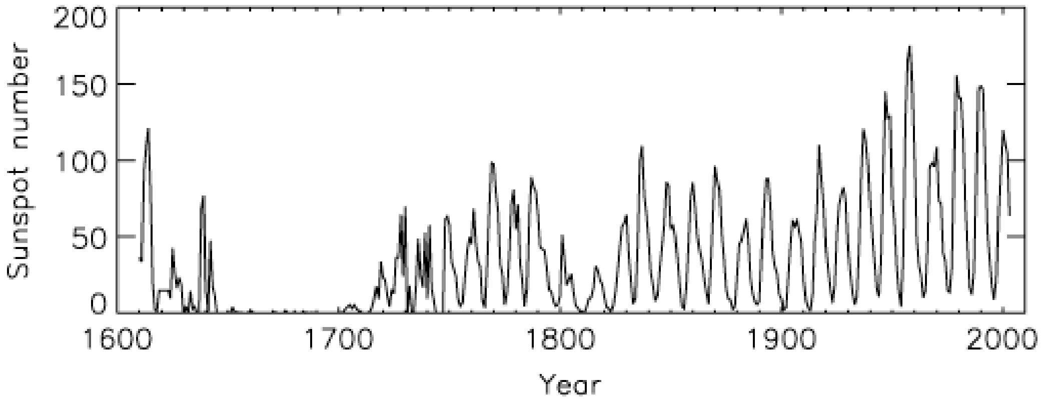

Fig. 1.1 The yearly averaged group sunspot number is shown [1]. Apart from the dominant solar cycle, there is a long-term modulation of sunspot activity along with extended periods of almost vanishing sunspots (1640-1700, Maunder minimum) or rather few sunspots (1800-1820, Dalton minimum).

Figure 1.1 demonstrates the current record of (yearly averaged) sunspot numbers. While the 11-year cycle is self-evident, there is also a balance of the sunspot activity on longer time scales. Most momentous is the second half of the 17th century (the Maunder minimum [2]), when sunspots were totally absent. We now realize that this is only one instance of the incidental "grand minima" of solar activity; a less marked case is the Dalton minimum at the start of the 19th century.

Sunspot latitudes, polarity rules and tilt angle of bipolar regions

The average latitudes of recently showing up sunspots show a deliberate variety over the span of the 11-year activity cycle. Sunspots emerge in two wide latitude belts, which are generally symmetric with respect to the solar equator. At the beginning of a cycle, these belts are centered around ±30° latitude. In the course of the cycle, the sunspot belts migrate towards the equator and reach about ±5° average latitude towards the end of the cycle. In a latitude-time graph of sunspot occurrence, this drift leads to a characteristic butterfly-shaped pattern, which is clearly visible in the related graph of the surface magnetic field (see figure 1.2).

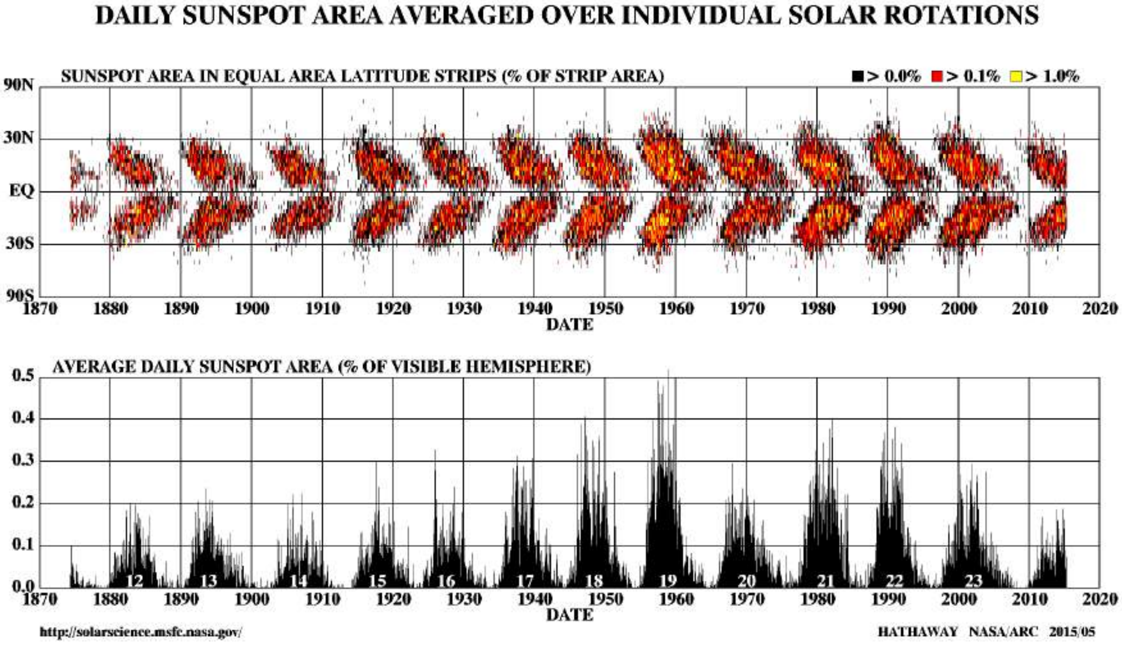

Fig. 1.2 *Top*: The butterfly diagram shows the latitudes of sunspots as a function of time, in particular exhibiting the evolution of these latitudes over the solar cycle. The combined effects of convection and meridional circulation lead to the magnetic flux transport to high latitudes and thus cause reversals of the polar magnetic fields in phase with the activity cycle. *Bottom*: The record of daily sunspot area. (Image courtesy: Dr. D Hathaway, MSFC, NASA)

Sunspots commonly show up in groups embedded in magnetically bipolar regions. In most cases, they share each other's local magnetic polarity. The bipolar regions are generally arranged in the East-West direction and their polarities are arranged as per the following polarity guidelines (Hale's law, first formulated on the basis of magnetic field measurements in sunspot groups [3]):

1. The magnetic orientation of bipolar regions remains the same in each hemisphere during an 11-year activity cycle.
2. The bipolar regions in the Northern and Southern hemispheres have the opposite magnetic orientation.
3. The magnetic orientation of the bipolar regions reverses from one cycle to the next.

1.1.2 Solar dynamo

The consistent inversions of the global magnetic field over the span of the solar cycle cycle demonstrate that induction effects by bulk flow of the electrically conducting plasma dominate over diffusion effects in deciding the evolution of the solar magnetic field. In the radiative zone, radially overturning movements are firmly suppressed by the exceptionally stable stratification and the rotation is almost rigid, with the goal to harbor just a gradually decaying fossil field (see, [4]). The magnetic fields responsible for solar cycle. Therefore, they originate in the overlying convection zone, where the convective motions and differential rotation lead to strong induction effects. The field reversals in the 11-year time span, which is amazingly short contrasted with the diffusion time scales, show that these flows need to provide mechanisms for both the fast generations and for the effective removal and dissipation of magnetic flux. While the latter procedure can be attributed to the radical enhancement of the effective magnetic diffusivity for a large-scale magnetic field by turbulent flows in the convection zone, the mechanisms for flux generation beginning from a little starting seed field is the essential issue of solar dynamo theory. Different conceivable outcomes have been viewed as and various models have been developed, yet a completely reliable and prescient theory is as yet deficient. Further in this section, a brief representation of the essential ideas on solar dynamo is given. More details about the theory can be found in [5, 6].

Basic Equations

In the system of magneto-hydrodynamics (MHD), the dynamo problem can be expressed as the quest for arrangements of the MHD equations (the combination of the non-relativistic

Maxwell equations, Ohm's law, and the hydrodynamic equations [7]) with non-vanishing magnetic energy as time goes to infinity. So as to these avoid trivial cases, the flow providing the induction effects is confined to a compact volume and must be consistent (finite kinetic energy and gradients). Besides, the magnetic field should not be maintained by sources (currents) at infinity [8, 9]. We can characterize a self-excited dynamo by the instability of the solution with vanishing magnetic field, a trivial solution of the MHD equations. The evolution of magnetic field, B, affected by a velocity field, u, and an magnetic diffusivity,η, is described by the induction equation,

$$\frac{\partial B}{\partial t} = \nabla \times (v \times B) + \eta \nabla^2 B \tag{1.1}$$

For dynamo action, the induction term (first term on the right-hand side) needs to overcome (globally) the diffusion term (the second term). Therefore, an important necessity for dynamo action is that the order-of-magnitude ratio of both terms, the magnetic Reynolds number, is greater than one.

Another fundamental prerequisite for a working dynamo results from Cowling's hypothesis, which states that a rotationally symmetric magnetic field (like a dipole field) can't be kept up by dynamo action under rather general circumstances [10]. Likewise, the solar magnetic field is clearly non-axisymmetric. Another important "anti-dynamo" theorem is because of Elsasser [11] and states that differential rotation alone (or, more generally, a simply toroidal motion in a development of the velocity field into spherical harmonics) can't drive a dynamo in a sphere, provided that the magnetic diffusivity is steady on cspherical surfaces [12, 13]. As an outcome of these limitations, a working dynamo requires a complex three-dimensional and non-axisymmetric structure of both the produced magnetic field and the driving velocity field.

In case of the Sun, differential rotation and convective flows are thought to be the most important elements of self-excited dynamo action. For high magnetic Reynolds numbers, the magnetic field lines are frozen to the fluid elements, so that the shearing effect of the latitudinal and radial gradients of the angular velocity of rotation leads to the generation and intensification of an azimuthal magnetic field (adjusted to the direction of rotation) from a meridional field with radial and latitudinal components (see left chart of figure 1.3). Elsasser's theorem demonstrates that differential rotation alone is not adequate to keep up the solar magnetic field; a flow regenerating the meridional part of the field is needed also. The conceptual premise for most convection-based models of this process is the Parker loop [14], which describes how convective upflows and downflows in a rotating system create meridional flux loops through twisting of the field lines because of the action of the Coriolis force on the flow (see right chart of figure 1.3). Upflows grow and downflows contract owing

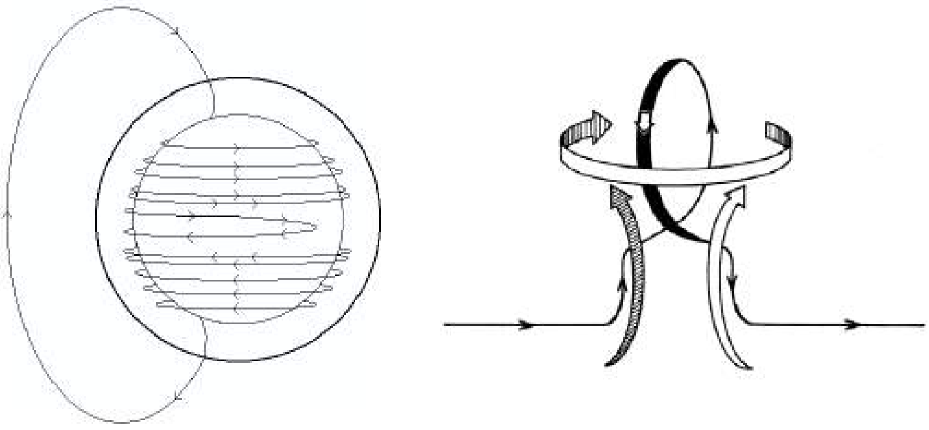

Fig. 1.3 *Left*: Generation of an azimuthal magnetic field through winding of meridional magnetic field lines by differential rotation. Sketched here is the case of a latitude-dependent angular velocity with a faster-rotating equatorial region (Image courtesy: Dr. David Hathaway, MSFC, NASA). *Right*: Sketch of the Parker loop [14].

to the pressure stratification of the convection zone. This leads to the same sense of twisting by the Coriolis force in one hemisphere and, reliably, to the inverse sense in the other side of the equator. For an azimuthal field of opposite polarity in both hemispheres as produced from a dipolar field by differential rotation (cf left graph of figure 1.3), the superposition of numerous such meridional loops shapes an large-scale meridional field of switched extremity regarding the first field from which the azimuthal field had been twisted up in any case. Hence, the Parker loop gives a straightforward clarification to the polarity reversals of the large-scale meridional field of the Sun. Regarding the twisting by differential rotation it prompts periodic reversal of both meridional and azimuthal magnetic field and subsequently represents the watched essential components of the solar cycle: large-scale field inversions and the polarity rules of sunspots groups(accepting that the recent begin from the azimuthal field segment).

The Parker mechanism escapes Cowling's restriction of a dynamo-generated axisymmetric field through the intrinsic non-axisymmetry of the loop development while the spatially averaged generated field may well have an overwhelming axisymmetric component.

1.1.3 Magnetic field in convection zone

In a convecting medium with large magnetic Reynolds number, magnetic flux is removed from areas of closed streamlines and amassed in flux concentration between the convection cells [15, 16]. This procedure of flux expulsion, which can be specifically seen in the flux distribution on the solar surface, prompts a firmly irregular distribution of the magnetic flux. By relationship and in addition through qualitative minimum-energy arguments [17] and numerical simulations [18], such irregularity of the magnetic field is additionally proposed to prevail all through the entire solar convection zone. The inquiry is whether irregular structures generated by flux expulsion can turn out to be adequately strong and large to decouple themselves from the convective velocity field to be represented by their inside dynamics. Sunspots are a sample of such a "autonomous" structure, yet observations demonstrate that they are not formed by flux expulsion by surface flows but rather develop as coherent (though at first divided) elements from underneath. Actually, the sunspot polarity rules and other systematic components indicate that the magnetic flux in the reason behind the development of sunspots and (large) bipolar regions is not commanded by non-stationary convective motion but rather starts from a source region of largely requested and azimuthally situated magnetic flux in the deep convection zone [19, 20]. These perceptions are as per the photo of a "rising tree" [21, 22]: strands of magnetic flux separate from the source area, ascend through the convection zone and rise at the surface in a powerfully dynamic manner to shape bipolar magnetic regions and sunspots. Strictly when the introductory phase of flux rise and subsequent to dividing into little scale flux fixations does the surface field come continuously affected by convective stream examples and large-scale surface streams, so that its large-scale advancement can be very much depicted by flux transport models.

Consequently, it is important to consider the progress of magnetic structures in the convection zone to make the association between the watched properties of the surface fields and the dynamo procedure producing the magnetic flux in any case.

1.2 Lower Atmosphere

The atmosphere of the sun is made out of several layers, essentially the photosphere, the chromosphere and the crown. It’s in these external layers that the sun’s energy, which has risen from the sun’s inside layers, is detected as sunlight.

The lowermost layer of the sun’s atmosphere is the photosphere. It is around 500 kilometers thick. This layer is the place the sun’s energy is discharged as light. Due to the separation from the sun to Earth, light reaches us in around eight minutes.

The photosphere is marked by bright, bubbling granules of plasma and darker, cooler sunspots, which develop when the sun’s magnetic field gets through the surface. Sunspots seem to move over the sun’s disk. Watching this movement drove space experts to understand that the sun rotates on its own axis. Since the sun is a wad of gas with no strong structure, distinctive regions rotate at diverse rates. The sun's central regions rotate in around 24 days, while the polar regions take over 30 days to make a complete rotation.

The photosphere is likewise the wellspring of solar flares: tongues of flame that develop a huge number of miles over the sun's surface. Solar flares produce blasts of X-beams, bright radiation, electromagnetic radiation and radio waves.

The surface of a star is characterized to have a temperature given by the effective temperature in the Stefan-Boltzmann law. By utilizing a straightforward model for stellar airs, accepting nearby warm harmony in a plane parallel geometry and the Eddington rough guess, the effective temperature of the sun can be indicated to happen at an optical profundity of 2/3. This shows the surface of a star is not at the highest point of the atmosphere where the optical depth is characterized as zero: Stars are seen at a profundity inside the atmosphere. Stars, with the exception of neutron stars, have no strong surface. Along these lines, the photosphere is ordinarily used to portray the Sun's or another star's visual surface.

The following layer is the chromosphere. The chromosphere emanates a reddish glow as super-heated hydrogen blazes off. Anyway, the red edge must be seen amid an aggregate solar eclipse. At different times, light from the chromosphere is typically excessively frail, making it impossible to be seen against the brighter photosphere.

1.2.1 Small-scale magnetic features

The magnetic field in the photospheric layers is concentrated in dynamic regions and in a system distributed over the entire Sun. In active regions (outside sunspots) the magnetic field is packed into pretty much discrete components that together form faculae or plage regions. In the peaceful Sun (i.e. outside active regions) the magnetic flux components shape a system outlining the borders of supergranular cells with a length size of 20-40 Mm. Another kind of magnetic feature in the quiet Sun are the between internetwork elements, which are situated in the insides of supergranular cells. On a more restricted scale, the magnetic elements forming faculae and the network, and likely additionally those in the internetwork, are situated in the downflow paths between granules [23, 24].

There is an entire range of magnetic features having altogether different sizes and properties on the solar surface. Sunspots are the biggest and rarest. Indeed, even now and again of most noteworthy solar activity they cover just a fraction of a percent of the solar surface. By and large littler than sunspots are pores, despite the fact that the largest pores can be greater than the littlest sunspots. Pores normally have measurements of a few thousand kilometers and are dim. They are recognized from sunspots by the way that they have no penumbra, showing up like confined umbrae [25]. Significantly littler, and much more regular, are magnetic elements, bright structures with diameters littler than a couple of hundred kilometers. High resolution obsrevations show magnetic features with sizes comfortable achievable spatial determination of 150 km [26]. In the quiet Sun, backhanded evaluations recommend the presence of features of the internetwork field with a measurement of, at the most, 50 km [27]. At long last, observations show an inescapable turbulent field in photospheric layers. The present photo of the magnetic elements is that they have numerous features just the same as sunspots (in spite of the fact that at first sight the distinctions may seem to command). Specifically, both structures, and additionally pores, are thought to be appearances of extraordinary concentration of magnetic flux and are typically depicted by the theory of magnetic flux tubes. Outlines of the properties of magnetic components can be found in [28, 29].

The magnetic structure in both active regions and in the peaceful Sun system is fundamentally the same: the magnetic field is moved into pretty much discrete elements of magnetic flux isolated by regions with relatively minimal magnetic flux (to first estimate they are thought to be sans field, despite the fact that they likely harbor a significant turbulent magnetic field). Consequently the measured intensity from a piece of the Sun can, utilizing a basic two-part model, be composed as

$$I_{obs} = fI_m + (1-f)I_b \tag{1.2}$$

where I_{obs} is the observed intensity, I_m the intensity of light from the magnetic component, I_b from the 'free field 'background and f is the magnetic filling factor, i.e. the fraction of the observed a piece of the solar surface secured by strong magnetic fields. Mathematical statement (7.1) is taking into account the supposition that the spectra of magnetic elements and background are the same all around, or, then again, it portrays average properties. One motivation behind why equation (7.1) has been broadly utilized is that numerous magnetic features are not determined by spectropolarimetric observations, which typically don't achieve the spatial resolution achievable in wide band pictures. In spite of the fact that I_m and I_b do, to a certain degree, rely on upon f , to first request on diverse parts of the Sun I_{obs} can be resolved just by changing f , while leaving I_m and I_b unaltered. At the point when considering the net polarization (as depicted by the Stokes parameters Q and U for net straight polarization and Stokes V for net round polarization) created by the Zeeman effect to first order.

$$S_{abs} = fS_m, \qquad whereS = Q, UandV \tag{1.3}$$

In actuality, the relationship is more intricate, however equation (7.2) does show one noteworthy point of interest of utilizing the polarized Stokes parameters when considering small scale magnetic elements, exceptionally when they are spatially unresolved: to first order the free-field atmosphere does not add to the polarized Stokes profiles.

1.3 Spectropolarimetry

The presence of a magnetic field can be found from the Zeeman splitting of spectral lines. Notwithstanding, this is conceivable just for an adequately strong field. If the field is weak, we must fall back on the way that the Zeeman components are polarized. We have as of now perceived how the resonance-scattering spectrometer and the magneto-optic channel use this polarization. In the present segment we shall depict the part and polarization of Zeeman components in the solar spectrum, and how the Zeeman effect can be utilized to concentrate data about the magnetic field in the region on the Sun where the spectral line has been shaped.

Zeeman splitting

We review that on account of a weak magnetic field (weak as in LS - or Russell-Saunders - coupling is the suitable portrayal) L, S, J, and M_J are the quantum numbers that characterize the condition of a particle. L describes the aggregate orbital angular momentum of the electrons (all the more absolutely: of the external electrons which are dealt with expressly), S is the analogue for the spin, and J for the total angular momentum; M_J is the 'magnetic 'quantum number that decides the part of the total angular momentum in any one direction (z, say), and embraces the qualities -J, -J +1, . . . J, while J itself can have the qualities |L - S|, |L - S| + 1, . . . L + S.

At the point when the strength of the field, B, is zero all M_J -states have the same energy. This degeneracy is removed if $B \neq 0$; the z-direction is then the course of the field vector B. For the energy shift and the subsequent Zeeman displacement of a spectral line the Landé component of every state,

$$g = 1 + \frac{J(J+1) + S(S+1) - L(L+1)}{2J(J+1)} \tag{1.4}$$

Let g, g'and M', M be the Landé factors and magnetic quantum numbers of the lower and upper states of the transition considered. Then the displacement of the line from its original position λ_0 is

$$\lambda - \lambda_0 = \frac{e}{4\pi c m_e} g * \lambda^2 B \tag{1.5}$$

where

$$g* = gM - g'M' \tag{1.6}$$

By and large there is a Zeeman multiplet, or anomalous splitting. Since solar lines are wide, the components of such a multiplet typically are not resolved. For a weak magnetic field it is conceivable to regard the multiplet as though it was a triplet. An effective g element is then figured from the g* estimations of the contributing parts; every component is given a weight as per its intensity.

The Zeeman triplet comprises of the two shifted σ components and the unshifted π part. At the point when the observable pathway is toward the magnetic field (the longitudinal Zeeman effect), the observer sees just the σ components, which have circular polarization of inverse sense. At the point when the observer looks in a direction opposite to B (the transverse Zeeman effect), he sees every one of the three components: the π component, linearly polarized perpendicular to B, and the σ parts, linearlyly polarized parallel to B.

These rules for the polarization of the tnormal Zeeman triplet are substantial for a absorption line beginning in an optically thin layer. For a line in emission, the sense of circular polarization is turned around, and (for the transverse Zeeman effect) 'perpendicular 'and 'parallel 'must be traded. The reason is of course that just emission lines have intensity by themselves, while what is found in an absorption lines is just the leftover intensity.

In the event that B is significantly smaller than in sunspots, or if B is practically identical with the sunspot field strength, however the field covers just a little fraction of the resolved region on the Sun, then the Zeeman effect is, best case scenario discernible as line increasing. However, the Zeeman components are polarized in any case regardless of how little the splitting is. Babcock and Kiepenheuer initially researched the likelihood of isolating the Zeeman components by method for polarimetric strategies in around 1950.

Polarized Light

Let us first consider a single monochromatic wave train of electromagnetic radiation, propagating in the z direction. The electric vector lies in the x-y plane:

$$E_x = \xi_x cos\phi \qquad E_y = \xi_y cos(\phi + \varepsilon) \tag{1.7}$$

where $\phi = \omega t - \kappa z$; ε is the phase difference between E_x and E_y; ξ_x and ξ_y are constant amplitudes which, together with ε, describe the state of polarization of the wave, which is elliptic in general. In 1852, G.G. Stokes defined the parameters for a polarized light.

$$I = \xi_x^2 + \xi_y^2, \qquad Q = \xi_x^2 - \xi_y^2, \qquad U = 2\xi_x\xi_y cos\varepsilon, \qquad V = 2\xi_x\xi_y sin\varepsilon \tag{1.8}$$

These guidelines for the polarization of the normal Zeeman triplet are legitimate for an absorption line starting in an optically thin layer. For an emission line, the feeling of circular polarization is turned around, and (for the transverse Zeeman effect) 'perpendicular'and 'parallel'must be exchanged. The reason is obviously that just emission lines have intensity without anyone else, while what is found in an absorption lines are simply the leftover intensity.

At the point when the observer is neither toward B nor in a direction perpendicular to B all the Zeeman components are seen. We shall treat this case beneath; we should then additionally drop the limitation that the spectral line begins in an optically thin layer.

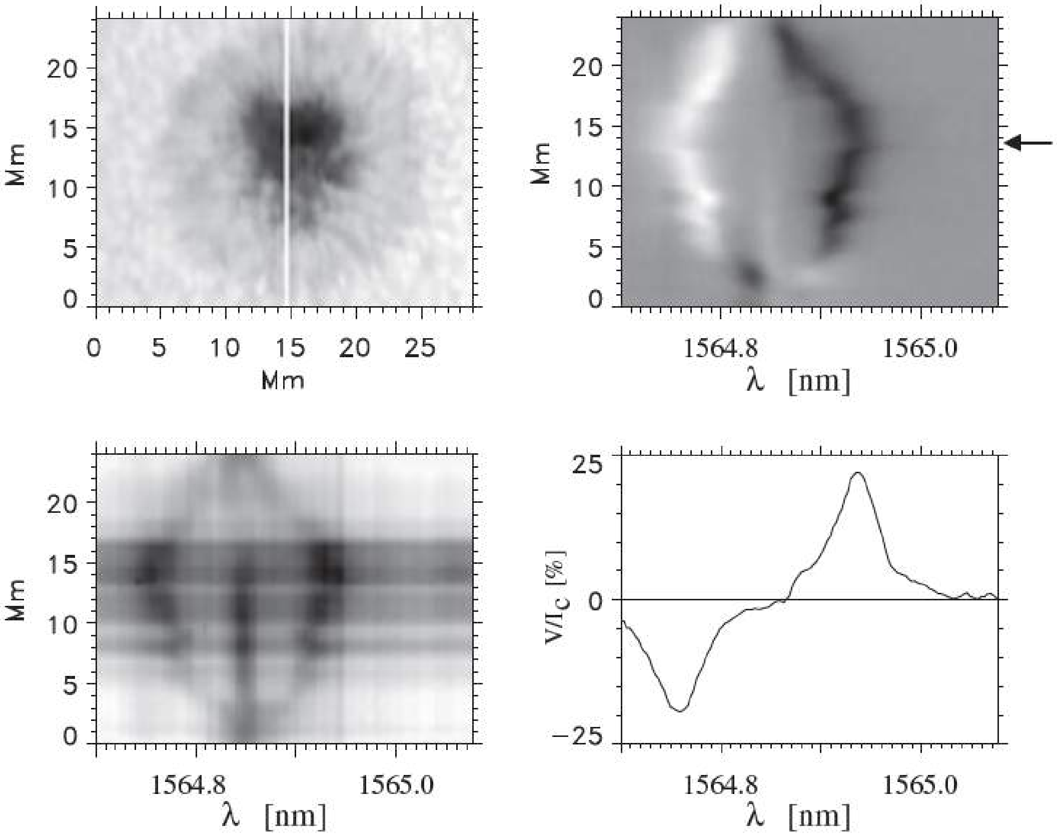

Fig. 1.4 Zeeman splitting and circular polarization of the Fe I line at 1564.8 nm. The correlation tracker is used to scan the sunspot image (upper left) across the entrance of the spectrograph; the white line is the slit position for the spectrum shown in the lower left. The upper right panel shows the circular polarization, with an arrow marking the position of the V (λ) profile in the lower right. Observation on 9 Nov 1999 at the German Vacuum Tower Telescope, Tenerife, with the infrared polarimeter TIP [30]

Solar spectral lines are Doppler and collision broadened. This has the result that the magnetic field B must be of order 0.15 T or larger before the Zeeman splitting can be perceived. Surely, Hale in 1908 found the magnetic field of sunspots by method for Zeeman splitting. As per equation (1.5) Zeeman splitting increments with expanding wavelength, $\triangle\lambda_B \propto \lambda^2$, while $\triangle\lambda_D \propto \lambda$; henceforth the division of the Zeeman components is seen all the more unmistakably in the infrared than in the noticeable. Sunspots by and large have fields up to ≈ 0.3 T. For most spectral lines this is still weak in the feeling of the LS coupling, so that (1.4) to (1.6) are appropriate.

Chapter 2

Instrumentation and Observation

2.1 Swedish Solar Telescope

The Swedish 1-m Solar Telescope (SST) on the island of La Palma, Spain, had first light with a halted down 60 cm opening on March 2, 2002 (see Figure 2.1). On May 21, the telescope was opened to full aperture and the adaptive optics system was used for the first time. As of now on the second day of operation it conveyed diffraction-restricted pictures, i.e. it came to the hypothetical resolution limit for a telescope of this size. This implies the SST has little optical abnormalities after remuneration by the adaptive optics system, intended to counter out blurring brought about by the atmosphere. This empowers solar stargazers to see and photo solar subtle elements of littler size than already conceivable.

The SST will address present and imperative inquiries concerning solar magnetic fields and the dynamics of the upper solar atmosphere and will likewise be utilized to enhance our comprehension of the arrangement of stellar spectra.

The front lens of the SST has a distance across of just shy of 1 meter, making it the largest optical solar telescope in Europe and the second on the planet, after the McMath-Pierce telescope in Arizona, USA. Situated on the best known site for solar telescopes on the planet, it can see subtle elements as little as 70 km on the solar surface. This obliges the utilization of an alleged versatile mirror that redresses for the obscuring created by the Earth's atmosphere 1000 times each second. The SST is the first solar telescope that is intended for utilization with such a mirror.

The SST is operated by the Institute for Solar Physics of the Royal Swedish Academy of Sciences but located within the Observatorio del Roque de los Muchachos of the Instituto de Astrofísica de Canarias on the island of La Palma, Spain. The SST replaces a previous 50 cm telescope that has been a world leading solar research instrument for over ten years.

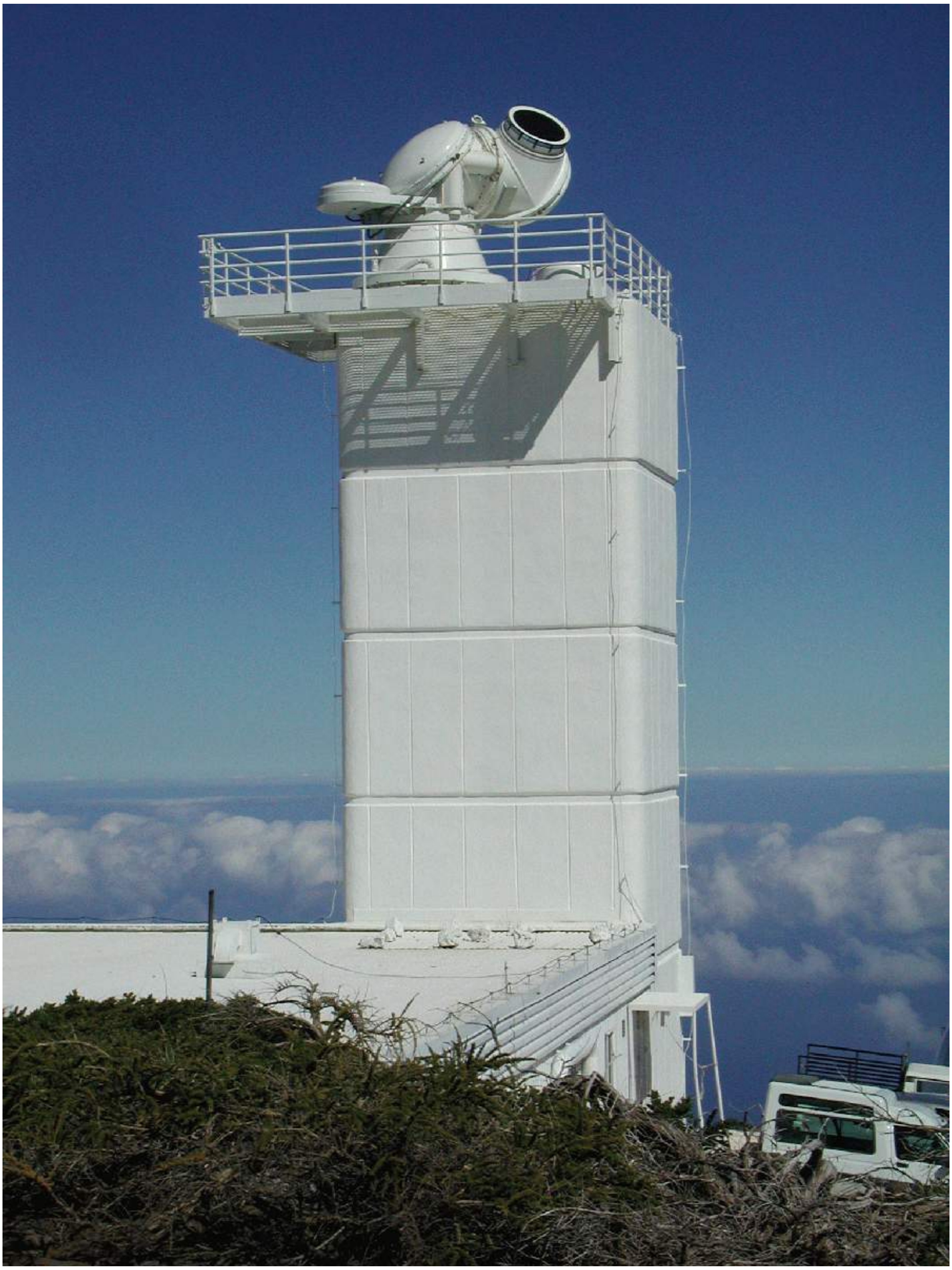

Fig. 2.1 Swedish 1-m Solar Telescope

2.2 CRISP

The CRisp Imaging SpectroPolarimeter (CRISP) is installed in the red beam and is usable from 510 to 860 nm. It consists of 0.3-0.9 nm wide pre-filters, liquid crystal (LC) modulation, a dual Fabry-Pérot (FP) tunable filter system, and a polarizing beam splitter located close to the final focal plane and feeding two 1k×1k-pixel Sarnoff CCD cameras. The FP system has a compact tele-centric optical design with a minimum number of optical surfaces and high overall transmission. MOMFBD image restoration is aided with a third CCD recording broad-band images through the pre-filter. All three cameras are synchronized by use of an external shutter.

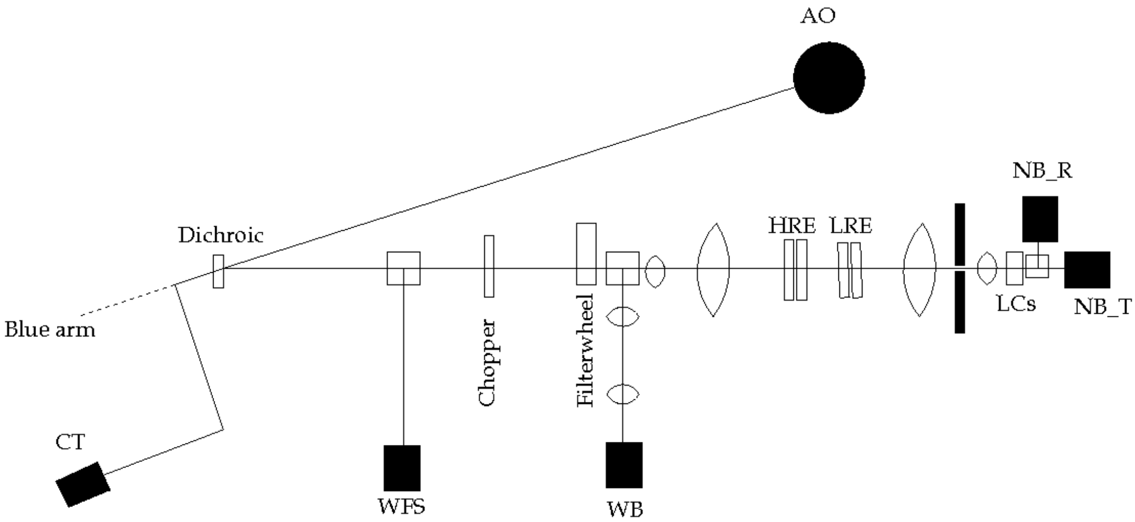

Fig. 2.2 Schematic drawing of CRISP Instrument. The signal from the Adaptive Optics (AO) enters into the Red arm through the dichroic mirror. WB - Wide Band Camera, HRE - High Resolution Etalon, LRE - Low Resolution Etalon, LCs - Liquid Crystals

2.3 Observations

We have observed the bright points (BPs) in the active region (AR) NOAA 11768 with the SST, located in La Palma. The observations have been made between 8:20 to 11:00 UT on 13 June 2013. The centre of the field of view (FOV) is at heliocentric distance of $\mu = 0.94$ (410X, -240Y). The seeing conditions were good to excellent (Figure 2.3), along with a few poor seeing.

The signal from the sun's photosphere has been detected by the CRisp Imaging SpectroPoalrimeter (CRISP; [31]) at the SST and a time sequence of full Stokes parameters have been acquired. The CRISP filter was set up to sample the photospheric Fe–I and C–I lines at

5250.2Å and 5380.0Å respectively, and one of the chromospheric Ca–II IR lines at 8542.0Å. All lines were observed in full-Stokes mode, with a cadence of approximately 30s. (TODO: wavelengths are to be verified) An overview of the observed lines is given in table 2.1

line	wavelength[Å]	FWHM[mÅ]	points
Fe–I	5250.0	50	12
C–I	5380.0	52	12
Ca–II	8542.0	80	??

Table 2.1 Observational parameters

The Adaptive Optics (AO) of SST reduces the blurring to some extent by deforming the mirror [32]. The signal enters into the CRISP instrument after the AO system. It is a dual Fabry-Pérot interferometer consisting of two etalons to select the wavelength of the signal. Two liquid crystal (LC) modulators are mounted behind the beam splitter to polarize the signal, in order to record the Stokes parameters with two 1k $\times$ 1k pixel Sarnoff CCD cameras. A third CCD camera was used to record the wide-band images. All these cameras are synchronized in order to allow post-facto image restoration. The images are reconstructed using multi-frame-multi-object-blind-deconvolution techniques (MOMFBD, [33]) to achieve a near diffraction limited spatial resolution (0."12).

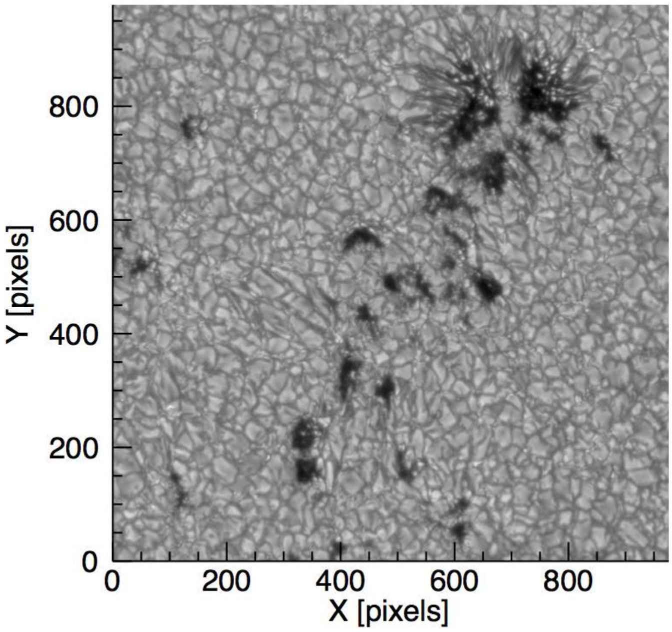

Fig. 2.3 Wide-band image of AR 11768 which is observed by the CRISP at a heliocentric angle of 20.45 ($\mu = 0.94$) on 13 June 2013 at 9:04 UT.

Each line observed has been recorded at 12 wavelength positions ($\lambda - \lambda_0$ = [-20, -16, -12, -8, -4, 0, +4, +8, +12, +16, +20, +24] pm). One complete spectral scan, including all the three lines, has been completed in 30 seconds.The full FOV of the observation covers an area of 55" $\times$ 55" with a plate scale of 0.”058 per pixel.

The data recorded have been reduced using the CRISPRED pipeline [34]. This streamlines the complex data reduction process and provides a science-ready data. The images observed in Fe I (525.0 nm) and C I (538.0 nm) have been aligned with the sub-pixel accuracy by cross-correlating the corresponding continuum images.

Chapter 3

Data Analysis

The analysis of the data that was recorded has been outlined in this chapter. Even with a very good seeing condition, we do not get a continuous sequence of good frames. The image restoration methods are used to improve them. In the later part of the chapter, the inverted parameter has been analyzed. One of the dynamic events have been chosen and its characteristics have been determined.

3.1 Image restoration

Even after using adaptive optics in the telescope, only low order aberrations are removed. But the high order aberrations are dealt with the image restoration methods. There are many algorithms developed for these ground based observations. The most commonly used are Speckle Interferometry [35, 36] and Phase Diversity methods [37, 38]. We have used the Multi-Object Multi-Frame Blind Deconvolution (MOMFBD) method [33]. The method has been discussed in more detail in section 3.1.2.

3.1.1 Seeing Error

The sun-rays have to pass through the atmosphere of earth to each the telescope situated on the ground. The optical density of the layers of atmosphere above the telescope is varying at every point and at every time. Thus, the speed of light will not be same for the whole wavefront. This deforms the wavefront causing blurring of images. The pattern of deformation is also not constant for a particular place because of the changing weather conditions. A schematic diagram of the wavefront distortion is shown in Figure 3.1.

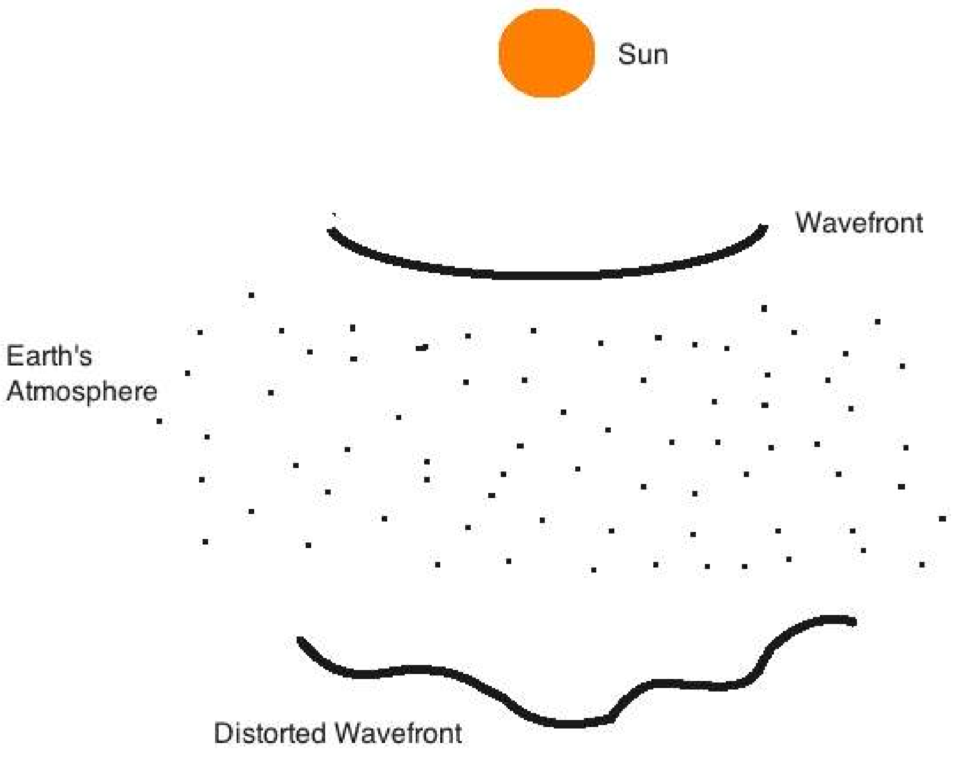
Sun
Wavefront
Earth's
Atmosphere
Distorted Wavefront

Fig. 3.1 The varying refractive index of the air in the atmosphere distorts the wavefront.

3.1.2 MOMFBD code

Images are restored from wavefront aberrations by means of the Multi-Object Multi-Frame Blind Deconvolution (MOMFBD; [33]) method, based on the algorithm by Löfdahl ([39]). Not using any assumptions about the aberration statistics, the method can compensate for optical aberrations, both from the atmosphere and from the optics, and partial compensation by the AO does not introduce any extra complexity.

The MOMFBD algorithm is based on the assumption that the aberrations are isoplanatic, so that the point spread function (PSF) is constant within the FOV. This makes it possible to find the PSF and deconvolve the raw data by use of fast Fourier transforms. In the process, each subfield is low-pass filtered individually based on the local signal-to-noise ratio (SNR). In order to make this assumption hold, at least approximately, the processing is done on overlapping subfields of a $\sim$5 arcseconds squared. The restored subfields are then mosaicked, resulting in a restored version of the entire FOV.

3.2 Event

The time sequence of the data was analyzed. The observed FOV contains a sunspot and many pores. This region is very active with flux emergence in many places. It can be observed from the elongated granules in Figure 1. The time sequence of Stokes parameters show many events occurring on the photosphere. Along with flux emergence, we see magnetic structures moving in the FOV. In some places, we see a train of wave traveling along the boundary of the structure. We have identified various regions in Stokes V images where the surface waves could be seen (Figure 3.2). The lifetime and size of each of the waves are different. We have selected one of these regions for our analysis, where the wave could be properly resolved and its lifetime is longer compared to others. The patch of the image where the wave is present has been inverted. The area of these new image frames is 9" × 9". This was done to make the inversion process faster because many scans were inverted in order to create a time sequence.

The inverted data of each scan is aligned to form a time sequence of the physical quantities. The 30th scan of the observed data has been assumed to be the first frame of the time sequence that has been analyzed. This was done because the seeing was not good in the initial frames.

The event (surface wave) was seen in the time sequence of images of magnetic field strength, temperature and magnetic field vector's inclination angle. But it was most clear in the LOS-magnetic field images, which was used to analyze the event.

The BPs, where the waves have been observed, have a magnetic field of about 1000 G. The oscillations are a sequence of train of wavelets that originate, grow, travel and then attenuate away. One of the wavelets has been selected which was most prominent in the

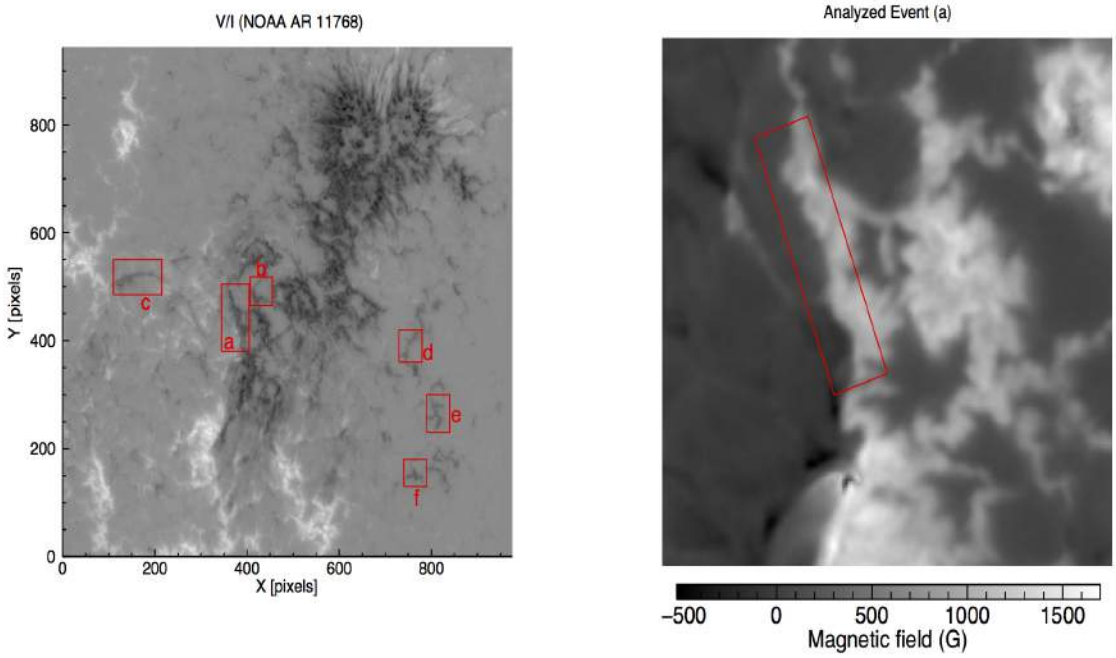

Fig. 3.2 The Stokes parameter V/I represents the circular polarization of the light that was observed. The image gives indication of the presence of surface waves in various small-scale magnetic structures. Some of the regions where it can seen are shown in the image with rectangular boxes. The region in box ’a’ has been inverted and analyzed in this paper because this wave sustains for longer period and is better resolved than others.*Analyzed Event.* This is the vertical magnetic field strength image of region in box ’a’. The interface where the wave is seen has been marked.

vertical magnetic field images. The wavelength of the wavelet is about 1200 km. The image of the event is shown in Figure 3.2. The initial growth of the oscillations was seen to be linear, which becomes non-linear with time. We have tried to explain the event in the linear regime of the event. The whole event in the observed time series sustains for about 50 minutes.

3.3 Inversion Code

To aide in the characterization of the wave-like phenomena, we have used the SPINOR code [40] to get values for the physical quantities of the observed FOV of the Sun's photosphere. This code is based on the STOPRO routines described by Solanki et al. [41]. The inversion code gives us the thermal, magnetic and velocity gradients with optical depth by using the strengths, shapes and asymmetries present in the Stokes profile [29, 42]. The stratification of each atmospheric parameter with the optical depth is calculated using a spline interpolation through the preset $\log(\tau)$ nodes, where the code can modify a pixel's atmosphere. The resultant full atmosphere is then used to solve the radiative transfer equation. The emergent synthetic spectra are fitted iteratively by Levenberg-Marquardt algorithm that minimizes the difference between the measured profile and the computed profile.

We have used the two lines, Fe I (525.0 nm) and C I (538.0 nm), together in the inversion code. These lines are very close to each other, which makes the inversion possible. We have been able to use more complex model atmosphere to get height dependent values for the parameters because we have more number of wavelength points.

3.4 Destretching

The interface on which the wave is observed is curved and tilted with respect to the edges of the image. We apply a coordinate transformation, which rotates and straightens the interface (see Figure 3.3).

This is complicated by the deformation of the interface, which is hard to distinguish from a bending of the interface itself. Although the interface is not completely stable in time, the transformation stabilizes the interface between the strongly and weakly magnetized regions sufficiently, so it can be analyzed in more detail.

In order to avoid removal of features, the interface was not fitted for on a frame by frame basis, but instead a single transformation was used to "straighten" and align all frames

$$x' = x \quad y' = y - ax^2 - bx - \frac{b^2}{4a}$$

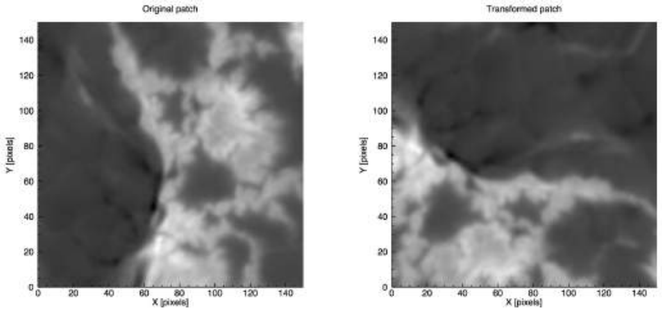

Fig. 3.3 The original patch is rotated by 119° in clockwise direction. In order to straighten the interface, the transformation applied is as follows: $x' = x$, $y' = y - ax^2 - bx - \frac{b^2}{4a}$ (where $a = 0.00125476, b = -0.520568$)

with $a = 0.00125476$, and $b = -0.520568$. Figure 3.3 shows the transformation from the original to the transformed form for one frame. This transformation is applied to all the images in the time series. For subsequent analysis, the horizontal velocity must also be transformed.

3.5 Horizontal velocity field

Since there are many rapidly moving features visible in the Stokes-V movie, it seems plausible that a substantial horizontal flow field is present in the FOV. To obtain the velocity vectors of this flow field, local correlation tracking (LCT) was performed on subsequent frames, using the method developed in Topka et al. [43]. Each frame in the time series was stretched onto the next frame, by hierarchically dividing the images in subframes, determining the optimal alignment by cross-correlation for each subframe, then sub-dividing again, and repeating the cross-correlation. This process is repeated until the sub-frames are too small to contain reliable structures useful for cross-correlation. The alignment displacements obtained in this way are easily converted in velocities by division with the time step between frames.

Figure 3.4 shows the velocity field obtained in this way, using the line-of-sight magnetic field $B\cos\gamma$. The horizontal velocity in most strong magnetic features appears to be low, at only a few hundred m/s, in line with the expected situation of ionized gas that is "frozen" onto the strong magnetic field, which is anchored firmly in the deep photosphere. The smaller, rapidly moving bipolar features, however, appear to be embedded in a larger scale horizontal flow of approximately 1-1.5 km/s, which is directed along the patches of strong magnetic field.

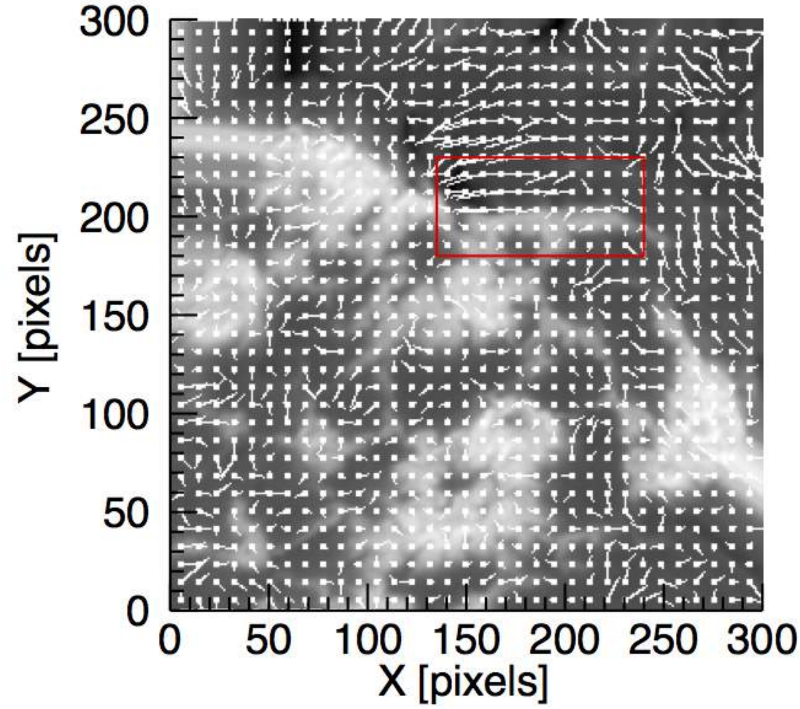

Fig. 3.4 The image shows the horizontal velocity vectors drawn over the vertical magnetic field strength. The horizontal velocity vectors are aligned along the interface of bright points (BPs). The magnitude is much higher than the horizontal velocity vectors inside the BPs.

To ensure this flow is not a purely magnetic flow, but is indeed also present in the weakly magnetized gas surrounding the magnetic features, the LCT was repeated on temperature and LOS-velocity maps. Although the results differ by up to 500m/s, the overall picture of a substantial flow, *shearing* the patches of strong flux consistently appears from all of them.

The height dependent solution of the temperature and velocity allow us to repeat the LCT at different optical depth surfaces, thus providing a rough estimate of the height dependence of the horizontal flow velocity. The values found suggest some dependence of the horizontal flow velocity on height, but with a very similar overall flow direction.

3.5.1 Shear velocity

To measure the "typical" change in the conditions across the interface, we try to produce an average for the physical quantities over a region just above, and just below the interface. The resulting average, still contains a lot of variation, both intrinsic, but also due to variations in

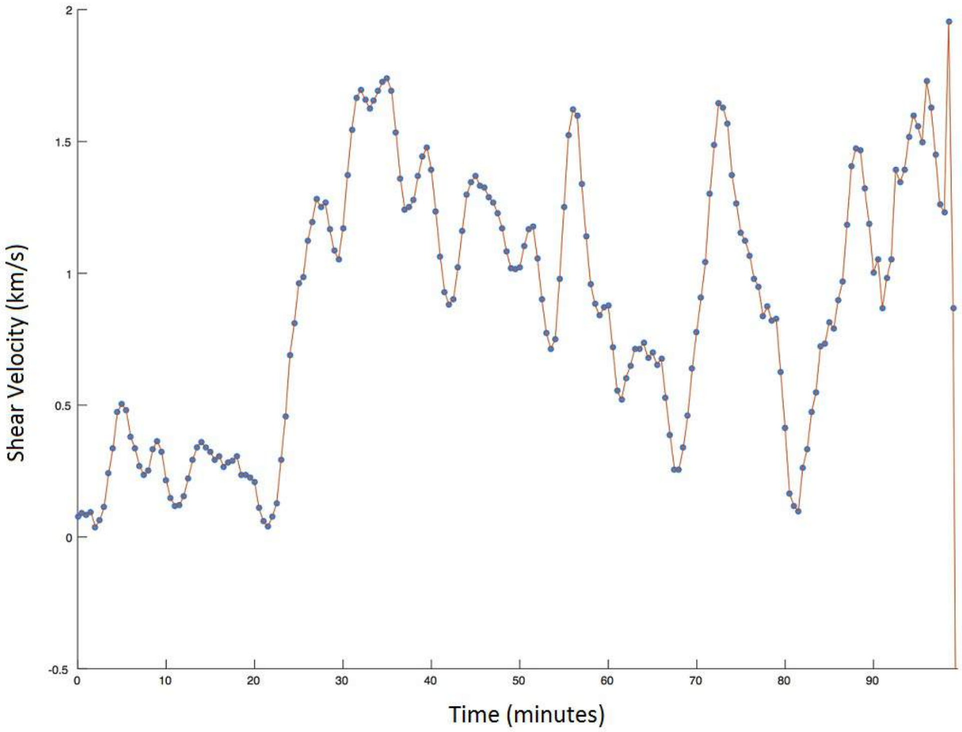

Fig. 3.5 The values plotted have been determined by taking the average of the velocities of plasma in the background region that is very close to the interface.

the seeing conditions. To reduce this variation, the averages over space were also averaged in time, resulting in the plot shown in Figure 3.5.

The shear velocity starts off with a value close to zero almost everywhere, in the initial phase of the observation sequence. At around minute 22, there is a distinct increase in the horizontal velocity in the weakly magnetized flux emergence region, while the weakly magnetized material remains largely at rest. The shear produced in this way is usually associated with Kelvin-Helmholtz (KH) instability, and from about minute 34, a perturbation of the interface (wave) can be observed. This first train of visible wavelets damp away by around minute 43, by which time Figure 3.5 shows that the velocity has decreased significantly. When the shear velocity goes up again, we see the next train of wavelets. This process goes on for about 50 minutes during the whole observation period.

3.5.2 Phase speed

The phase velocity of the wavelet is determined by tracking one maximum of the perturbed interface, as illustrated in Figure 3.6.

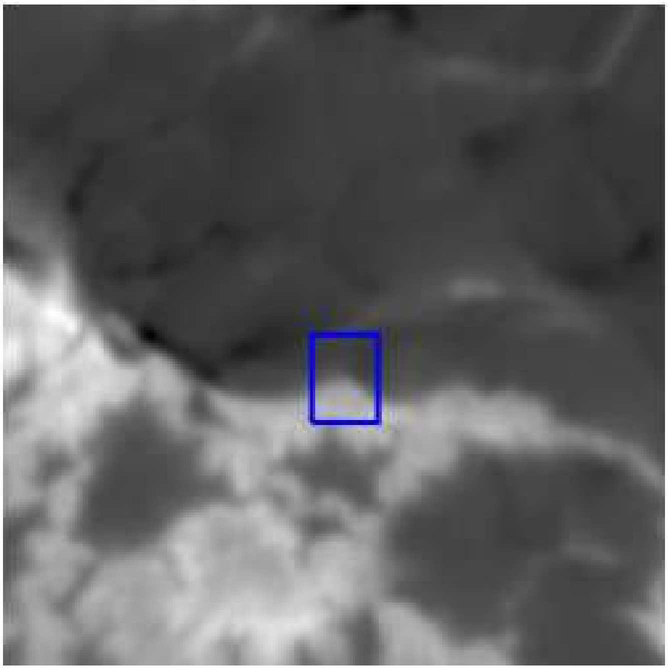

Fig. 3.6 The part of the wavelet marked by a box is tracked in order to get the phase velocity.

Figure 3.7 shows the measured phase velocity as a function of time, in the time frame it can be measured. In particular in the middle part, the phase speed is remarkably constant, at 1.5 km/s. This value is quite close to the value of the horizontal shear flow and is probably directly proportional to the shear velocity.

3.6 Amplitude growth

The amplitude of the wavelet is difficult to define, as the interface equilibrium position is not really known. We define the amplitude therefore as the maximum deviation of the interface from the mean position in time. To determine the amplitude of the wavelet accurately, a curve was fitted to the interface between the strongly and weakly magnetized regions by taking the spatial derivative of B_v. As there is a strong gradient of the magnetic field strength at the interface, we have taken the gradient of the patch where the interface is seen.

After finding the curve that defines the interface, the distance between the maxima and minima points is found. The amplitude is half of this distance. Few of the images were of poorer quality and the interface could not be determined by taking the gradient of the image. For the amplitude is these poor frames, we have used linear interpolation.

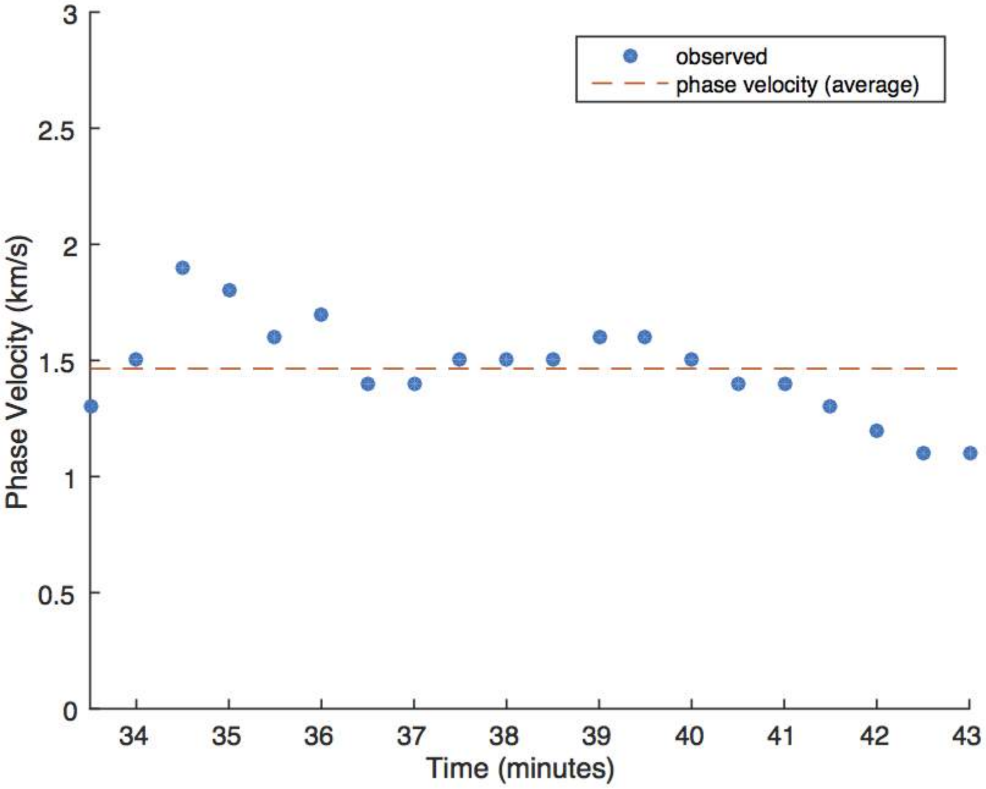

Fig. 3.7 The average phase velocity from the observed data is 1.465 km/s.

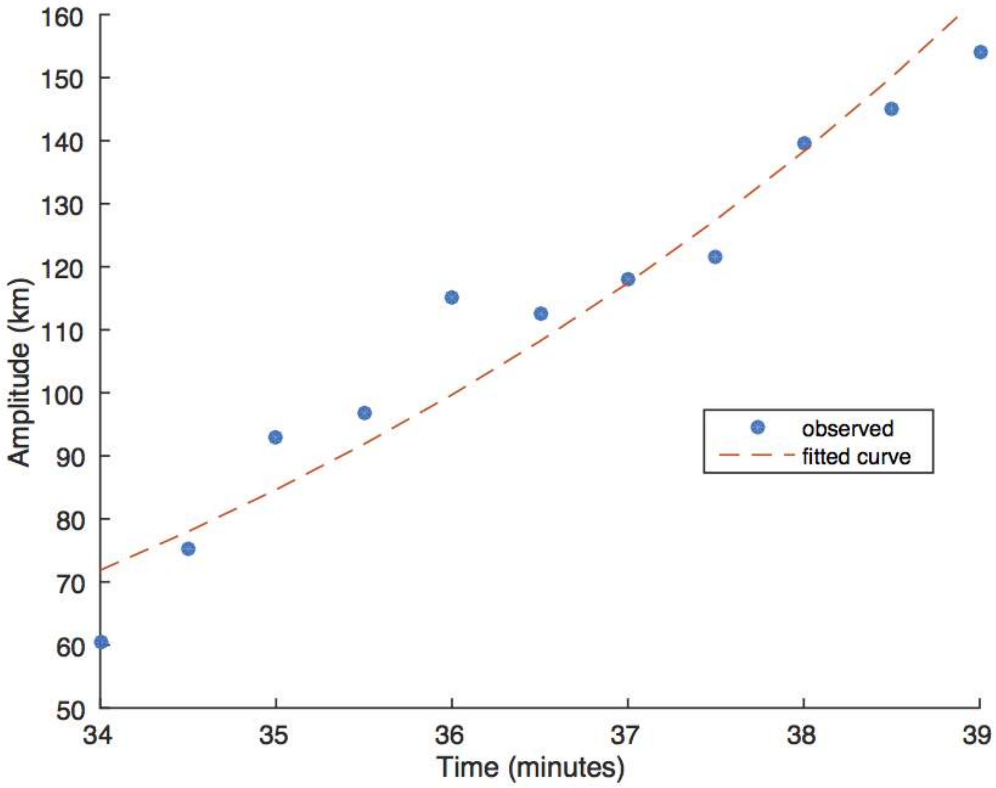

Fig. 3.8 The exponential curve fitted to the observation is $A(t) = 71.86e^{0.164(t-t_\circ)}$. Here, $t_\circ = 34 minutes$.

The initial growth of the oscillations was seen to be linear, which becomes non-linear with time. We have tried to explain the event in the linear regime of the event.

We have considered the global maximum of the wavelet for determining the amplitude. The amplitude of the wavelet is not uniform. We see a amplitude growth during the initial phase of the event and it damps away after some time. The amplitude of the wavelet is plotted as a function time during the growth (Figure 10). We could not detect the magnitude below a certain value because of limits on the resolution of image. As for any instability, we expect this growth to be exponential. We have fitted an exponential curve into the amplitude values. The curve was found to be $A(t) = 71.86e^{0.164(t-t_\circ)}$, where $t_\circ$ is the start time of observation.

Chapter 4

Theoretical model

In this chapter, the basic equation and theory behind the structure and evolution of plasma in the solar atmosphere has been outlined. The set of equations which govern the magnetized plasma on the Sun are known as magnetohydrodynamics (MHD) and the foundations of MHD theory has been outlined. Additionally, the instabilities that can occur in a plasma has been explained. Finally the model that could explain the observed event has been present.

4.1 Magnetohydrodynamic Theory

The evolution and structure of the solar atmosphere is dictated by the interaction of the solar plasma with the magnetic field [44]. These interactions are governed by a set of equations known collectively as magnetohydrodynamics (MHD). They are called so because they are a combination of the equations of electric and magnetic fields and those of fluid dynamics. This section contains a brief summary of these equations and the approximations used to model the changing magnetic features of the solar atmosphere.

Electromagnetism equations

The Maxwell's equations govern the interaction between electric and magnetic field. The equations are as follows,

$$\nabla . E = \frac{\rho}{\varepsilon} \tag{4.1}$$

$$\nabla \times E = -\frac{\partial B}{\partial t} \tag{4.2}$$

$$\nabla . B = 0 \tag{4.3}$$

$$\nabla \times B = \mu j + \mu \varepsilon \frac{\partial E}{\partial t} \tag{4.4}$$

In the set of equations given above, B is the magnetic field, E is the electric field, j is the current density, μ is the magnetic permeability in the vacuum, ε is the permittivity of the free space and ρ is the plasma density.

Along with the Maxwell's equation, we consider the generalized Ohm's law,

$$j = \sigma(E + v \times B) \tag{4.5}$$

Assuming the velocity of plasma much less than the speed of light, the second term of the right hand side of Ampere's law (Equation 4.4),

$$\nabla \times B = \mu j \tag{4.6}$$

The value of j is replaced in the Ampere's law, which has been determined by rearranging the Ohm's law (Equation 4.5). From this, the value for E becomes,

$$E = -v \times B + \frac{1}{\mu \varepsilon} \nabla \times B \tag{4.7}$$

The above value for E is used to eliminate it from Faraday's law (Equation 4.2) to give the induction equation,

$$\frac{\partial B}{\partial t} = \nabla \times (v \times B) + \eta \nabla^2 B \tag{4.8}$$

where $\eta = \frac{1}{\mu \varepsilon}$ is called the magnetic diffusivity.

The induction equation controls the electromagnetic property of the plasma. This is one of the MHD equations.

Fluid Equations

The mass continuity equation states that plasma can neither be created nor destroyed. It is given as,

$$\frac{\partial \rho}{\partial t} = \nabla . \rho v \tag{4.9}$$

Here, ρ is the plasma density and v the velocity. If the plasma is incompressible ($\frac{D\rho}{Dt} = 0$), then, with the use of vector identities, the mass continuity equation (Equation 4.9) reduces to,

$$\nabla.v = 0 \tag{4.10}$$

The equation of motion is given by,

$$\rho \frac{\mathrm{D}v}{\mathrm{D}t} = -\nabla P + F \tag{4.11}$$

where P is the pressure and F the external forces. $\frac{\mathrm{D}}{\mathrm{D}t}$ is the convective time derivative.

$$\frac{\mathrm{D}}{\mathrm{D}t} = \frac{\partial}{\partial t} + \nabla.v \tag{4.12}$$

The external forces that govern a plasma system are the magnetic (Lorentz), the gas pressure and the gravitational forces. The equation of motion is then,

$$\rho \frac{\mathrm{D}v}{\mathrm{D}t} = -\nabla P + j \times B + \rho g \tag{4.13}$$

The above equation is called the Navier-Stokes equation for plasma fluids. Finally, there is the energy equation, which for the case of F = 0 has the following form [45],

$$\frac{\partial \varepsilon}{\partial t} + \nabla.[v(\varepsilon + p)] = 0 \tag{4.14}$$

where,

$$\varepsilon = \frac{\rho v^2}{2} + \frac{p}{\gamma - 1} \tag{4.15}$$

It is the total energy density. The first term is kinetic energy and the second term is internal energy. γ denotes adiabatic index. By using the mass-continuity equation, the energy equation can be written as,

$$\frac{\partial p}{\partial t} + v.\nabla p = -\gamma p \nabla.v \tag{4.16}$$

The three important equations (Equation 4.9, 4.13, 4.16) along with the Induction equation (Equation 4.8) and the solenoidal condition (Equation 4.3) are called the MHD equation. These equations govern the motion and characteristics of plasma fluid.

Linear Perturbation in MHD equations

We consider the instability that we observe to be linear perturbation in the system. The higher order perturbation would make the analysis more rigorous. In order to keep it simple, we consider a linear disturbance. Now we can write the physical quantities as:

$\rho = \rho_0 + \rho', p = p_0 + p', v = v_0 + v', B = B_0 + B'$. Then, the ideal linearized MHD equations for an adiabatic condition are as follows,

$$\frac{\partial \rho'}{\partial t} + v_0.\nabla\rho' + \rho_0\nabla.v' = 0 \tag{4.17}$$

$$\rho_0\frac{\partial v'}{\partial t} + \rho_0(v_0.\nabla)v' + \nabla(p' + \frac{1}{\mu_0}B_0.B') - \frac{1}{\mu_0}(B_0.\nabla)B' = 0 \tag{4.18}$$

$$\frac{\partial p'}{\partial t} + (v_0.\nabla)p' + \gamma p_0\nabla.v' = 0 \tag{4.19}$$

$$\frac{\partial B'}{\partial t} + (v_0.\nabla)B' - (B_0.\nabla)v' + B_0(\nabla.v') = 0 \tag{4.20}$$

$$\nabla.B' = 0 \tag{4.21}$$

The event has been observed in solar photosphere. It is very close to an adiabatic system with $\gamma = 5/3$.

4.2 Plasma Instability

An important field of plasma physics is the stability of the plasma. It usually only makes sense to analyze the stability of a plasma once it has been established that the plasma is in equilibrium. 'Equilibrium 'asks whether there are net forces that will accelerate any part of the plasma. If there are not, then 'stability 'asks whether a small perturbation will grow, oscillate, or be damped out.

In many cases a plasma can be treated as a fluid and its stability analyzed with magnetohydrodynamics (MHD). MHD theory is the simplest representation of a plasma, so MHD stability is a necessity for stable devices to be used for nuclear fusion, specifically magnetic fusion energy. There are, however, other types of instabilities, such as velocity-space instabilities in magnetic mirrors and systems with beams. There are also rare cases of systems, e.g. the Field-Reversed Configuration, predicted by MHD to be unstable, but which are observed to be stable, probably due to kinetic effects.

List of plasma instability

1. Bennett pinch instability (also called the z-pinch instability)
2. Beam acoustic instability

3. Bump-in-tail instability
4. Buneman instability
5. Cherenkov instability
6. Chute instability
7. Coalescence instability
8. Collapse instability
9. Counter-streaming instability
10. Cyclotron instabilities
11. Kelvin-Helmholtz fluid instability
12. Disruptive instability (in tokamaks)
13. Double emission instability
14. Drift wave instability
15. Edge-localized modes
16. Electrothermal instability
17. Farley-Buneman instability
18. Fan instability
19. Filamentation instability
20. Firehose instability (also called Hose instability)

4.2.1 MHD instability

Plasma beta is a ratio of the plasma pressure over the magnetic field strength.

$$\beta = \frac{p}{p_{mag}} = \frac{nk_B T}{(\frac{B^2}{2\mu_0})} \tag{4.22}$$

MHD stability at high beta is crucial for a compact, cost-effective magnetic fusion reactor. Fusion power density varies roughly as β^2 at constant magnetic field, or as β_N^4 at constant bootstrap fraction in configurations with externally driven plasma current. (Here $\beta_N = \frac{\beta}{(I/aB)}$ is the normalized beta.) In many cases MHD stability represents the primary limitation on beta and thus on fusion power density. MHD stability is also closely tied to issues of creation and sustainment of certain magnetic configurations, energy confinement, and steady-state operation. Critical issues include understanding and extending the stability limits through the use of a variety of plasma configurations, and developing active means for reliable operation near those limits. Accurate predictive capabilities are needed, which will require the addition of new physics to existing MHD models. Although a wide range of magnetic configurations exist, the underlying MHD physics is common to all. Understanding of MHD stability gained in one configuration can benefit others, by verifying analytic theories, providing benchmarks for predictive MHD stability codes, and advancing the development of active control techniques.

The most fundamental and critical stability issue for magnetic fusion is simply that MHD instabilities often limit performance at high beta. In most cases the important instabilities are long wavelength, global modes, because of their ability to cause severe degradation of energy confinement or termination of the plasma. Some important examples that are common to many magnetic configurations are ideal kink modes, resistive wall modes, and neoclassical tearing modes. A possible consequence of violating stability boundaries is a disruption, a sudden loss of thermal energy often followed by termination of the discharge. The key issue thus includes understanding the nature of the beta limit in the various configurations, including the associated thermal and magnetic stresses, and finding ways to avoid the limits or mitigate the consequences. A wide range of approaches to preventing such instabilities is under investigation, including optimization of the configuration of the plasma and its confinement device, control of the internal structure of the plasma, and active control of the MHD instabilities.

4.2.2 Kelvin-Helmholtz instability

The Kelvin-Helmholtz instability (after Lord Kelvin and Hermann von Helmholtz) can occur when there is velocity shear in a single continuous fluid, or where there is a velocity difference across the interface between two fluids. An example is wind blowing over water: The instability manifests in waves on the water surface. More generally, clouds, the ocean, Saturn's bands, Jupiter's Red Spot, and the sun's corona show this instability.

The theory predicts the onset of instability and transition to turbulent flow in fluids of different densities moving at various speeds. Helmholtz studied the dynamics of two fluids of different densities when a small disturbance, such as a wave, was introduced at the boundary connecting the fluids.

In gravity, for a continuously varying distribution of density and velocity (with the lighter layers uppermost, so that the fluid is RT-stable), the dynamics of the KH instability is described by the Taylor-Goldstein equation and its onset is given by a Richardson number, *Ri*. Typically the layer is unstable for $Ri < 0.25$. These effects are common in cloud layers. The study of this instability is applicable in plasma physics, for example in inertial confinement fusion and the plasma-beryllium interface.

4.3 Proposed model

We consider the Bright Points (BP) region to be a region of magnetized plasma on the Sun's surface, with magnetic field (B) lines perpendicular to it (along z axis). The magnitude of magnetic field in the BP (denoted as B_i) is around 1000 G and the magnetic field of the background (B_e) is assumed to be negligible. The plasma inside the BP region is fully ionized with density ρ_i and pressure P_i, surrounded by plasma of density ρ_e and pressure P_e. The interface where the event occurs is assumed to be along the y-axis and the velocity discontinuity occurs at x=0. The horizontal flow of plasma (v) is assumed to be along the y-axis (Figure 4.1).

The sum of gas pressure and the magnetic pressure should not change drastically at the interface for an equilibrium state [46].

$$\frac{\mathrm{d}}{\mathrm{d}x}(p+\frac{B^2}{2\mu})=0 \tag{4.23}$$

The total sum of pressure is represented as p_{tot}. We consider the total pressure perturbation to be sinusoidal ($p'_{tot} = p^{\circ}_{tot}(x)e^{i(\kappa y-\omega t)}$) and solve the linearized MHD equations, we get an equation similar to one given by Miura & Pritchett [47].

$$\frac{\mathrm{d}^2 p^{\circ}_{tot}}{\mathrm{d}x^2} - \kappa\frac{\mathrm{d}p^{\circ}_{tot}}{\mathrm{d}x}R_{\circ}(x,\omega,\kappa) - \kappa^2 p^{\circ}_{tot}F_{\circ}(x,\omega,\kappa) = 0 \tag{4.24}$$

where

$R_{\circ} = \frac{\frac{1}{\kappa}\frac{\mathrm{d}}{\mathrm{d}x}\{\rho_{\circ}(x)[\frac{\omega}{\kappa}-v_{\circ y}]^2\}}{\rho_{\circ}(x)[\frac{\omega}{\kappa}-v_{\circ y}]^2}$ and $F_{\circ} = \frac{[\frac{\omega}{\kappa}-v_{\circ y}]^2-C_A^2-C_S^2}{C_A^2+C_S^2}$

Alfvén speed, $C_A^2 = \frac{B_{\circ z}^2}{\mu\rho_{\circ}(x)}$

Sound speed, $C_S^2 = \frac{\gamma p_{\circ}(x)}{\rho_{\circ}(x)}$

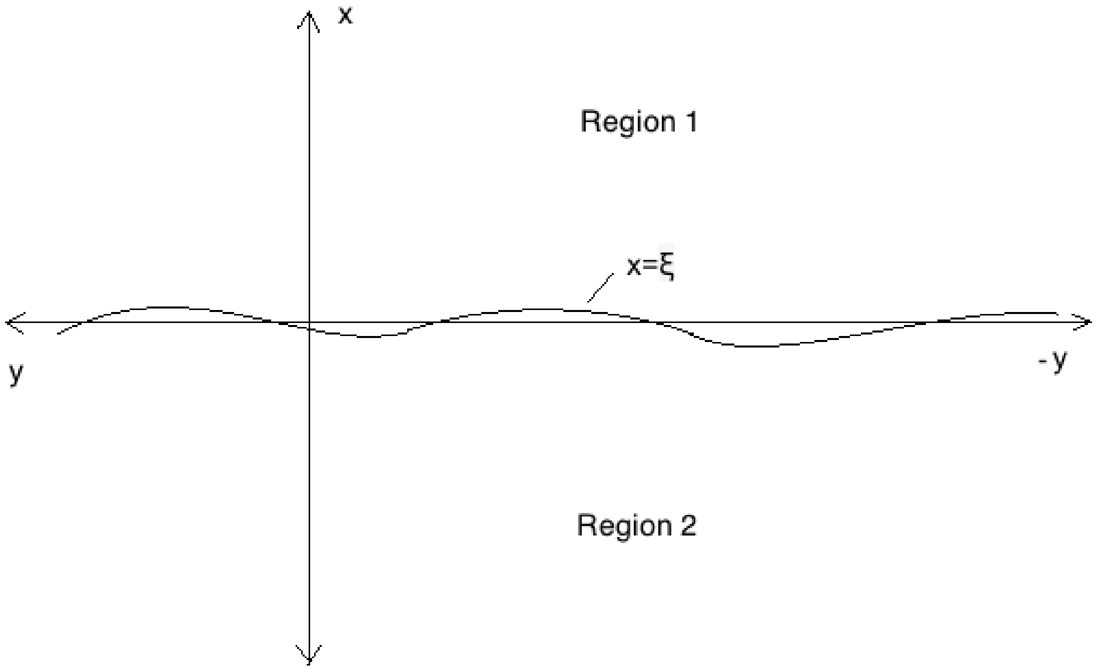

Fig. 4.1 The region 1 shown here is the background and region 2 is the bright points. The observed wave travels towards the left direction (+y). The shear velocity $v = v\hat{y}$ is the velocity of plasma in region 1. The magnetic field is perpendicular to these coordinate axes. It has a constant value in both regions. $B_i \sim 1000G$ and $B_e \sim 100G$. The perturbed interface shown in the diagram is given by the equation, $x = \xi$.

From the observations, we find that the density remains almost constant except at the boundary. The value of $v_{\circ y}$ is zero when x<0 and v when x>0. Thus, we consider $R_{\circ}$ to be negligible for each region. The solution of equation (8) can then be given as,

$$p_{tot}^{\circ} = C_1 e^{k\sqrt{F_{\circ}}x} + C_2 e^{-k\sqrt{F_{\circ}}x} \tag{4.25}$$

where

$$F_{\circ} = \left\{ \begin{array}{l} \frac{C_{Ai}^2 + C_S^2 - [\frac{\omega}{\kappa}]^2}{C_{Ai}^2 + C_S^2}, x < 0 \\ \frac{C_{Ae}^2 + C_S^2 - [\frac{\omega}{\kappa} - v]^2}{C_{Ai}^2 + C_S^2}, x > 0 \end{array} \right\}.$$

The magnetic field in the surrounding of the BP is very low as compared to the magnetic field inside BP. Thus, the Alfvén speed inside the BP is about 30 km/s whereas it is about 6 km/s in the outside region. The sound speed is almost same in both the BP region and the surrounding. The total pressure should have a finite value at infinity. Thus, the p_{tot}° for both regions can be given as,

$$p_{tot}^{\circ} = \begin{cases} C_1 e^{k\sqrt{F_{\circ}}x}, x < 0 \\ C_2 e^{-k\sqrt{F_{\circ}}x}, x > 0 \end{cases} \tag{4.26}$$

The total pressure should be equal at the interface. By using these boundary conditions for p_{tot}°, we get $C_1 = C_2 = C$ and the expression for perturbation of total pressure due to the KH instability,

$$p_{tot}' = \begin{cases} Ce^{\kappa\sqrt{F_{\circ}}x + i(\kappa y - \omega t)}, x < 0 \\ Ce^{-\kappa\sqrt{F_{\circ}}x + i(\kappa y - \omega t)}, x > 0 \end{cases} \tag{4.27}$$

In the above expression, 'C' is the amplitude of p_{tot}' at the interface. In order to calculate the perturbation of the interface layer, we consider x=ξ to be the curve formed when the interface gets perturbed. This quantity is related to the perturbation in velocity in the x direction by the following equation,

$$(\frac{\partial}{\partial t} + v_{\circ y}\frac{\partial}{\partial y})\xi = v_x' \tag{4.28}$$

By considering a sinusoidal curve for the interface layer, we get the expression for ξ.

$$\xi = \left\{ \begin{array}{l} \frac{\sqrt{F_{\circ}}p_{tot}^{\circ}}{\rho_{\circ}\kappa(\frac{\omega}{\kappa})^2} e^{i(\kappa y - \omega t)}, x < 0 \\ \frac{\sqrt{F_{\circ}}p_{tot}^{\circ}}{\rho_{\circ}\kappa(\frac{\omega}{\kappa} - v)^2} e^{i(\kappa y - \omega t)}, x > 0 \end{array} \right\}. \tag{4.29}$$

The perturbation at the interface (x=0) should give the same from both the equations for x>0 and x<0. This condition gives the dispersion relation.

$$\frac{1}{(\frac{\omega}{\kappa}-v)^2(C_S^2+C_{Ae}^2)}-\frac{1}{(\frac{\omega}{\kappa})^2(C_S^2+C_{Ai}^2)}=\frac{1}{(\frac{\omega}{\kappa}-v)^4}-\frac{1}{(\frac{\omega}{\kappa})^4} \tag{4.30}$$

The dispersion relation derived here is a fifth-order equation, which cannot be solved analytically. We use the values of shear velocity, sound speed and Alfvén speed from the observation and solve equation numerically.

Chapter 5

Discussion

The main result of this study is the first observation of well resolved surface waves along the magnetic structure. This may be an evidence for the presence of waves caused by Kelvin-Helmholtz instability, which has been discussed in literature previously (cf. [48, 49]).

5.1 Numerical calculation

The dispersion equation (4.30) that has been derived in the previous chapter cannot be solved analytically. There are many root finding algorithms, like, Newton's method, Muller's method etc.

The method required should be able to solve n-order equations. The algorithm used here is a combination of bisection, secant, and inverse quadratic interpolation methods. The method is discussed in more detail in the book by Brent [50].

5.2 Observation and model

The proposed model is based on solving the MHD equations for a plasma system where there is KH instability. There are many literature on this topic [49, 51, 52]. We have tried to model the first train of wavelets that is seen between 34th to 43rd minute of observation. The strength of magnetic field vector along the interface is very low in this layer of the solar atmosphere. The magnetic field lines are mostly perpendicular to the interface. The shear velocity is about 1.7 km/s. This velocity value satisfies the critical velocity condition given by Chandrasekhar [51]. When the dispersion equation (13) is solved numerically, we get 6 solution for $\frac{\omega}{\kappa}$.

$$\frac{\omega}{\kappa} = \begin{cases} 0.85 \\ 8.33 \\ -3.88 + 6.85i \\ -3.88 - 6.85i \\ 0.85 + 0.84i \\ 0.85 - 0.84i \end{cases} \tag{5.1}$$

The value considered for $C_{Ae} = 6km/s$, $C_{Ai} = 30km/s$ and $C_S = 6km/s$. As we observe a growing wavelet, the solution that we consider for $\frac{\omega}{\kappa}$ would 0.85+0.84i or -3.88+6.85i. The latter is not possible because the phase velocity of the wavelet cannot be in the opposite direction to the shear velocity. The value of the calculated phase velocity that we got is 0.85 km/s, which is close to the observed value, i.e., 1.465 km/s under the observational condition. The imaginary part of ω gives the exponential growth rate of the wavelet. The wavelength of the wavelet has been observed to be 1200 km. This gives the imaginary part of ω as 0.264 min^{-1}. This value is also very close to the value of exponential growth that we had got from the curve fitted to the observed amplitude value (0.164 min^{-1}). The fitted curve is shown in Figure 3.8.

5.3 Further Implications

Any disturbance that occurs at the lower atmosphere affects the upper atmosphere. The flux-tubes acts as a medium for the disturbance to travel. In this case, we observe a disturbance that causes waves. These waves can use the flux-tubes as the wave-guide and travel upwards. The energy that the waves in the photosphere have can be transferred to the corona. This might be an explanation to the coronal heating problem.

Further study of the implications of this waves require an improvement in the instrument that is used for observation. The number of frames has to be increased. This can be done by using a Fast Polarimeter. The height dependent data has to be improved. We have tried to improve the height dependent parameters by using multiple spectral lines. Still, the images were not reliable because the displacement of the wave in the upper layer would be very small.

References

[1] D. V. Hoyt and K. H. Schatten. Group Sunspot Numbers: A New Solar Activity Reconstruction. *Sol. Phys.*, 179:189–219, 1998.

[2] J. A. Eddy. The Maunder Minimum. *Science*, 192:1189–1202, June 1976.

[3] G. E. Hale and S. B. Nicholson. The Law of Sun-Spot Polarity. *ApJ*, 62:270, November 1925.

[4] H. C. Spruit. Dynamo action by differential rotation in a stably stratified stellar interior. *A&A*, 381:923–932, January 2002.

[5] P. Charbonneau. Dynamo Models of the Solar Cycle. *Living Reviews in Solar Physics*, 2:2, June 2005.

[6] M. Ossendrijver. The solar dynamo. *A&A Rev.*, 11:287–367, 2003.

[7] A. R. Choudhuri. *The physics of fluids and plasmas : an introduction for astrophysicists /*. November 1998.

[8] H. K. Moffatt. *Magnetic field generation in electrically conducting fluids*. 1978.

[9] F. Krause and K.-H. Raedler. *Mean-field magnetohydrodynamics and dynamo theory*. 1980.

[10] T. G. Cowling. The magnetic field of sunspots. *MNRAS*, 94:39–48, November 1933.

[11] W. M. Elsasser. Induction Effects in Terrestrial Magnetism Part I. Theory. *Physical Review*, 69:106–116, February 1946.

[12] D. J. Ivers and R. W. James. Antidynamo theorems for non-radial flows. *Geophysical and Astrophysical Fluid Dynamics*, 40:147–163, 1988.

[13] M. R. E. Proctor. An extension of the Toroidal Theorem. *Geophysical and Astrophysical Fluid Dynamics*, 98:235–240, March 2004.

[14] E. N. Parker. The Generation of Magnetic Fields in Astrophysical Bodies. I. The Dynamo Equations. *ApJ*, 162:665, November 1970.

[15] E. N. Parker. Kinematical Hydromagnetic Theory and its Application to the Low Solar Photosphere. *ApJ*, 138:552, August 1963.

[16] N. O. Weiss. The Expulsion of Magnetic Flux by Eddies. *Royal Society of London Proceedings Series A*, 293:310–328, August 1966.

[17] E. N. Parker. Stellar fibril magnetic systems. I - Reduced energy state. *ApJ*, 283:343–348, August 1984.

[18] A. Brandenburg, I. Procaccia, and D. Segel. The size and dynamics of magnetic flux structures in magnetohydrodynamic turbulence. *Physics of Plasmas*, 2:1148–1156, April 1995.

[19] M. Schüssler. On the structure of magnetic fields in the solar convection zone. In T. D. Guyenne and J. J. Hunt, editors, *ESA Special Publication*, volume 220 of *ESA Special Publication*, pages 67–76, November 1984.

[20] M. Schüssler. Magnetic flux tubes and the solar dynamo - storage, instability and eruption of magnetic flux. In K. C. Tsinganos and A. Ferrari, editors, *NATO Advanced Science Institutes (ASI) Series C*, volume 481 of *NATO Advanced Science Institutes (ASI) Series C*, pages 17–37, 1996.

[21] C. Zwaan. On the Appearance of Magnetic Flux in the Solar Photosphere. *Sol. Phys.*, 60:213–240, December 1978.

[22] C. Zwaan. The evolution of sunspots. In J. H. Thomas and N. O. Weiss, editors, *NATO Advanced Science Institutes (ASI) Series C*, volume 375 of *NATO Advanced Science Institutes (ASI) Series C*, pages 75–100, 1992.

[23] A. M. Title, T. D. Tarbell, and K. P. Topka. On the relation between magnetic field structures and granulation. *ApJ*, 317:892–899, June 1987.

[24] S. K. Solanki. The origin and the diagnostic capabilities of the Stokes V asymmetry observed in solar faculae and the network. *A&A*, 224:225–241, October 1989.

[25] R. Keppens. *Sunspot Pores*, page 2043. November 2000.

[26] C. U. Keller. Resolution of magnetic flux tubes on the sun. *Nature*, 359:307, September 1992.

[27] H. Lin. On the Distribution of the Solar Magnetic Fields. *ApJ*, 446:421, June 1995.

[28] H. C. Spruit, M. Schuessler, and S. K. Solanki. *Filigree and flux tube physics*, pages 890–910. 1991.

[29] S. K. Solanki. Smallscale Solar Magnetic Fields - an Overview. *Space Science Reviews*, 63:1–188, March 1993.

[30] R. Schlichenmaier and M. Collados. Spectropolarimetry in a sunspot penumbra. Spatial dependence of Stokes asymmetries in Fe I 1564.8 nm. *A&A*, 381:668–682, January 2002.

[31] G. B. Scharmer. Comments on the optimization of high resolution Fabry-Pérot filtergraphs. *A&A*, 447:1111–1120, March 2006.

[32] G. B. Scharmer, M. Shand, M. G. Lofdahl, P. M. Dettori, and W. Wei. Workstation-based solar/stellar adaptive optics system. In P. L. Wizinowich, editor, *Adaptive Optical Systems Technology*, volume 4007 of *Society of Photo-Optical Instrumentation Engineers (SPIE) Conference Series*, pages 239–250, July 2000.

[33] M. van Noort, L. Rouppe van der Voort, and M. G. Löfdahl. Solar Image Restoration By Use Of Multi-frame Blind De-convolution With Multiple Objects And Phase Diversity. *Sol. Phys.*, 228:191–215, May 2005.

[34] J. de la Cruz Rodríguez, M. G. Löfdahl, P. Sütterlin, T. Hillberg, and L. Rouppe van der Voort. CRISPRED: A data pipeline for the CRISP imaging spectropolarimeter. *A&A*, 573:A40, January 2015.

[35] C. R. de Boer, F. Kneer, and A. Nesis. Speckle observations of solar granulation. *A&A*, 257:L4–L6, April 1992.

[36] O. von der Luehe. Speckle imaging of solar small scale structure. I - Methods. *A&A*, 268:374–390, February 1993.

[37] R. A. Gonsalves. Phase retrieval and diversity in adaptive optics. *Optical Engineering*, 21:829–832, October 1982.

[38] M. G. Löfdahl and G. B. Scharmer. Wavefront sensing and image restoration from focused and defocused solar images. *A&AS*, 107:243–264, October 1994.

[39] M. G. Löfdahl. Multi-frame blind deconvolution with linear equality constraints. In P. J. Bones, M. A. Fiddy, and R. P. Millane, editors, *Image Reconstruction from Incomplete Data*, volume 4792 of *Society of Photo-Optical Instrumentation Engineers (SPIE) Conference Series*, pages 146–155, December 2002.

[40] C. Frutiger, S. K. Solanki, M. Fligge, and J. H. M. J. Bruls. Properties of the solar granulation obtained from the inversion of low spatial resolution spectra. *A&A*, 358:1109–1121, June 2000.

[41] S. K. Solanki, C. Keller, and J. O. Stenflo. Properties of solar magnetic fluxtubes from only two spectral lines. *A&A*, 188:183–197, December 1987.

[42] J. O. Stenflo. Limitations and Opportunities for the Diagnostics of Solar and Stellar Magnetic Fields. In G. Mathys, S. K. Solanki, and D. T. Wickramasinghe, editors, *Magnetic Fields Across the Hertzsprung-Russell Diagram*, volume 248 of *Astronomical Society of the Pacific Conference Series*, page 639, 2001.

[43] K. P. Topka, T. D. Tarbell, and A. M. Title. High-resolution observations of changing magnetic features on the sun. *ApJ*, 306:304–316, July 1986.

[44] D. E. Osterbrock. The Heating of the Solar Chromosphere, Plages, and Corona by Magnetohydrodynamic Waves. *ApJ*, 134:347, September 1961.

[45] E. Toro. Riemann solvers and numerical methods for fluid dynamics. *Springer*, 1999.

[46] P. M. Edwin and B. Roberts. Wave propagation in a magnetically structured atmosphere. III - The slab in a magnetic environment. *solphys*, 76:239–259, March 1982.

[47] A. Miura and P. L. Pritchett. Nonlocal stability analysis of the MHD Kelvin-Helmholtz instability in a compressible plasma. *Journal of Geophysical Research*, 87:7431–7444, September 1982.

[48] R. A. Gerwin. Stability of interface between two fluids in relative motion. *Rev. Mod. Phys.*, 40:652, 1968.

[49] I. C. Rae. The MHD Kelvin-Helmholtz instability in the solar photosphere. *A&A*, 126:209–215, September 1983.

[50] R. Brent. Algorithms for Minimization Without Derivatives. *Prentice-Hall*, 1973.

[51] S. Chandrasekhar. *Hydrodynamic and hydromagnetic stability*. 1961.

[52] A. K. Sen. Stability of Hydromagnetic Kelvin-Helmholtz Discontinuity. *Physics of Fluids*, 6:1154–1163, August 1963.